IDEA League

Inversion of ERT data including uncertainties using the FE and RB methods

Niklas Krings

August 10, 2018

Inversion of ERT data including uncertainties using the FE and RB methods

for the degree of Master of Science in Applied Geophysics at

Delft University of Technology

ETH Zürich

RWTH Aachen University

by

Niklas Krings

August 10, 2018

Department of Geoscience & Engineering	·	Delft University of Technology
Department of Earth Sciences	·	ETH Zürich
Faculty of Georesources and Material Engineering	·	RWTH Aachen University

TUDelft

Delft University of Technology

IDEA LEAGUE
JOINT MASTER'S IN APPLIED GEOPHYSICS

Delft University of Technology, The Netherlands
ETH Zürich, Switzerland
RWTH Aachen, Germany

Dated: *August 10, 2018*

Committee Members:

_____

Prof. Florian Wellmann Ph.D.

_____

Dr. Cédric Schmelzbach

Supervisor(s):

Prof. Dr. Florian Wellmann

Denise Degen, M.Sc.

Rhea von Bülow, M.Sc.

Eidesstattliche Versicherung

_____   _____
Name, Vorname   Matrikelnummer (freiwillige Angabe)

Ich versichere hiermit an Eides Statt, dass ich die vorliegende Arbeit/Bachelorarbeit/ Masterarbeit* mit dem Titel

_____

_____

_____

selbständig und ohne unzulässige fremde Hilfe erbracht habe. Ich habe keine anderen als die angegebenen Quellen und Hilfsmittel benutzt. Für den Fall, dass die Arbeit zusätzlich auf einem Datenträger eingereicht wird, erkläre ich, dass die schriftliche und die elektronische Form vollständig übereinstimmen. Die Arbeit hat in gleicher oder ähnlicher Form noch keiner Prüfungsbehörde vorgelegen.

_____   _____

Ort, Datum   Unterschrift

*Nichtzutreffendes bitte streichen

Belehrung:

§ 156 StGB: Falsche Versicherung an Eides Statt

Wer vor einer zur Abnahme einer Versicherung an Eides Statt zuständigen Behörde eine solche Versicherung falsch abgibt oder unter Berufung auf eine solche Versicherung falsch aussagt, wird mit Freiheitsstrafe bis zu drei Jahren oder mit Geldstrafe bestraft.

§ 161 StGB: Fahrlässiger Falscheid; fahrlässige falsche Versicherung an Eides Statt

(1) Wenn eine der in den §§ 154 bis 156 bezeichneten Handlungen aus Fahrlässigkeit begangen worden ist, so tritt Freiheitsstrafe bis zu einem Jahr oder Geldstrafe ein.

(2) Straflosigkeit tritt ein, wenn der Täter die falsche Angabe rechtzeitig berichtigt. Die Vorschriften des § 158 Abs. 2 und 3 gelten entsprechend.

Die vorstehende Belehrung habe ich zur Kenntnis genommen:

_____   _____

Ort, Datum   Unterschrift

Abstract

The inversion process of data sets acquired with the electrical resistivity tomography can be a computational expensive calculation, because it requires a lot of forward simulations. Since computational resources are limited, the inversion for large field surveys can require immense computing times. One approach for reducing the computing times of forward simulations is the reduced basis method. It splits the problem into a parameter-dependent and parameter-independent part, which allows a precomputation of the parameter-independent part to speed up the calculation. Since the method of reduced basis has not been applied for the problem of electrical resistivity tomography so far, the question arises if and how it is applicable for this problem. Therefore, I performed forward simulations of the electrical potential distribution using the finite elements method and simulations using the reduced basis method for comparing the results. The methods give similar results, but unfortunately deviations above 1×10^{-4} occurred, while the error tolerance of the reduced basis method is set to 1×10^{-5}. Since the reduced basis method has been successfully applied on other applications, I assume that the problem is in my reduced basis simulation and can be solved by more fine tuning. By comparing the computing times of the simulations, a speed-up of 109.512 is achieved by using the reduced basis method. Furthermore, the pay-off is reached after 8.803 simulations. During the project, I noticed that only considered the resistivities of the subsurface as a varying parameter in the reduced basis is not sufficient. The source position needs to be a variable parameter in simulations of the electrical resistivity tomography, as well. This is necessary to tap the full potential of the reduced basis method in the application of the electrical resistivity tomography. The reduced basis method gives significant speed-ups and therefore, it has the potential to reduce the computing times of electrical resistivity tomography inversions.

Acknowledgements

Table of Contents

List of Figures

Acronyms

BERT Boundless Electrical Resistivity Tomography

DREAM Differential Evolution Adaptive Metropolis

ERT Electrical Resistivity Tomography

FD finite difference

FE finite element

FV finite volume

MCMC Markov Chain Monte Carlo

PDE Partial Differential Equation

POD Proper Orthogonal Decomposition

RB reduced basis

Chapter 1

Introduction

In geophysics, the limitations of the currently available computational resources have been an issue since the beginning of computer-aided calculations. And the demand for more computational resources probably will never be satisfied, because the processing of measured data and the modelling or simulation of physical systems can always be extended in the level of detail. Furthermore, there exist applications, that require the problem to be solved multiple times with varying parameters like an uncertainty quantification or a sensitivity analysis. Another intention to reduce the computational effort is make such calculations possible on mobile computers. This offers the possibility to perform data processing, which requires forward simulations, quickly in the field to evaluate the result. This could help to optimize the measurements and their parameters for obtaining the best possible result. Additionally, such faster computation enables real time processing of measured data. All in all, the need to reduce the computing time of calculations is omnipresent. One option for speeding up simulations is the reduced basis (RB) method. The idea of the method is to separate the problem into a parameter-dependent and a parameter-independent part. This allows the parameter-independent part to be precomputed and the computation of the problem with a different parameter can be performed faster.

In this thesis, the RB method will be applied to Electrical Resistivity Tomography (ERT) data. ERT surveys are used for obtaining a model of the near subsurface based on its resistivity. At first, synthetic data are generated and inverted. The purpose of this back-and-forth-process is to investigate the induced uncertainties by the inversion process with the aid of an uncertainty quantification. On the base of the inversion result a model is generated, which is used for forward simulations using on the one hand the finite element (FE) method and the RB method on the other hand. In the original plan of this project, the final step was to perform with these two forward simulations an inversion and the uncertainty quantification. Unfortunately, the limited time did not allow to perform either an inversion nor an uncertainty quantification. With these large computations the required computational effort of the two methods should have been compared. This should have given proper answers on the question, how the RB method can be useful for ERT problems.

The inversion of ERT data is a process, which requires multiple forward simulations. It is the most crucial step in the processing of measured ERT data. The measurements contain only apparent resistivities and the inversion is necessary for obtaining the actual resistivities. In this process multiple forward simulations are performed. Commonly, the inversion is done with FE inversion as, for example, implemented in the software package Boundless Electrical Resistivity Tomography (BERT) [Rücker et al., 2006][Günther et al., 2006]. This state of the art method is described in [Rücker et al., 2006] and [Günther et al., 2006]. The forward simulations there are done using the FE method. Other approaches use the finite difference (FD) method (see [Wei and Versteeg, 2008]). Wei also shows the need for an improved computational efforts for the inversion of ERT data. There, they implement an approach to speed up the computation by splitting each simulated dipole-dipole measurement into two measurements using a single current electrode and combining the results [Wei and Versteeg, 2008].

The RB method has previously been applied to thermal conduction problems and elasticity problems (see [Hesthaven et al., 2016], [Prud'Homme et al., 2002] and [Boyaval et al., 2009]). Additionally, Casenave (2015) applied the RB method on aeroacoustic problems (see [Casenave et al., 2015]). Other applications are transport problems in biomedical research. So, Rozza applied the RB method for simulations for the flow control of bypass configurations (see [Rozza, 2005b] and [Rozza, 2005a]). Inverse problems also have been addressed using the RB method. Lassila applied the RB method in cardiovascular mathematics by replacing the finite element solution by a reduced-basis approximation [Lassila et al., 2013]. Manzoni utilized the RB method to obtain an efficient numerical solution of statistical inverse problems in blood flows [Manzoni et al., 2014]. Furthermore, the RB method has been applied to electromagnetics. On the one hand Maxwell's equations were modelled with the aid of the RB method [Chen et al., 2009][Chen et al., 2010]. On the other hand it has been implemented for the electric field integral equation for parameterized scattering problems [Fares et al., 2011][Hesthaven et al., 2012]. The research done on the RB method itself focuses mostly on the convergence (see [Binev et al., 2011] and [Buffa et al., 2012]) and improvement of the error bounds (see [Veroy et al., 2003]).

Uncertainty quantification is a useful tools for analysing data. It has no limitation to a certain application and can be applied to data form various fields of science. For example, the method is used for investigating the simulations for predicting the outcome of medical surgeries (see [Schiavazzi et al., 2016]). Another application for uncertainty quantification is for example image reconstruction. So, Bardsley tried to reconstructed blurred images using the Markov Chain Monte Carlo (MCMC) method (see [Bardsley, 2012]). Furthermore, it has been used for data of orbits of extrasolar planets. The uncertainty quantification is used to determine which simulation describes the measured radial velocities of extrasolar planetary systems (see [Ford, 2005]). Therefore, Ford applies the MCMC uncertainty quantification. MCMC is a commonly used method and is a Bayesian approach [Adams et al., 2014]. But due to issues of efficiency, alternative method evolved like the Differential Evolution Adaptive Metropolis (DREAM) method, which tries optimize the performance of the MCMC method [Vrugt et al., 2009]. Since uncertainty quantifications require multiple forward simulations and efficiency is an issue, the RB method can be helpful tool to speed up the computation of uncertainty quantifications.

At the beginning of this thesis, I will focus on the theory behind the applications and the methods themselves. At first geoelectric surveys and especially the ERT will be explained in Section 2-1, followed by the inversion process. The next section describes the FE

approximation, with its basis functions in Section 2-2. The RB method will be explained in Section 2-3. Additionally, I will explain the theory of uncertainty quantification in Section 2-4. After that, the general workflow of the thesis will be illustrated in Section 3-1 and the used model is described in Section 3-2. Additionally, the employed software and their techniques will be discussed in Section 3-3. The results will be presented in Chapter 4. Furthermore, I will discuss my results in Chapter 5.

Chapter 2

Theory

At the beginning, I describe the essentials of the theory in the following. The theory behind the electrical resistivity tomography (ERT) is described in Section 2-1. Furthermore, the finite element (FE) method is explained in Section 2-2, followed by the reduced basis (RB) method. Finally, the theory behind uncertainty quantification is given in Section 2-4.

2-1 Electrical Resisitivity Tomography

In this chapter, the principles of ERT will be explained. At first, the electrical properties of the Earth are in the focus (Section 2-1-1), followed by the concept (Section 2-1-2) and the common survey arrays of ERT (Section 2-1-3). In the last section the inversion of ERT data is explained (Section 2-1-4).

2-1-1 Electrical properties of the Earth

The Earth and its rocks have electrical properties as any other material. Therefore, it is also possible to investigate the subsurface by exploiting variations in its electrical properties. Most geoelectrical applications search either for differences in the electrical resistivity ρ or the electrical permittivity ϵ. Surveys investigating the permittivity use usually electromagnetic methods, while direct current measurements are used to survey ρ. Anomalies in the subsurface with high contrasts in these properties to its surroundings can be well surveyed. Therefore, the most suitable investigation objects are orebodies and groundwater. The orebodies usually reveal a high contrast due to its high conductive metals. For example, sulfide ores of iron, copper and nickel. In the groundwater, solved ions show a significant conducting property. So, the groundwater appears as an electrolyte [Lowrie, 2007]. Most surveys use active sources, but there are also methods utilizing natural currents, also telluric currents. Their occurrence has two origins. Electrical currents in the ionosphere, originated from solar emissions, induce electromagnetically currents in the Earth's crust and upper mantle. Furthermore, electrochemical reactions in the subsurface can generate currents. Distinguishing
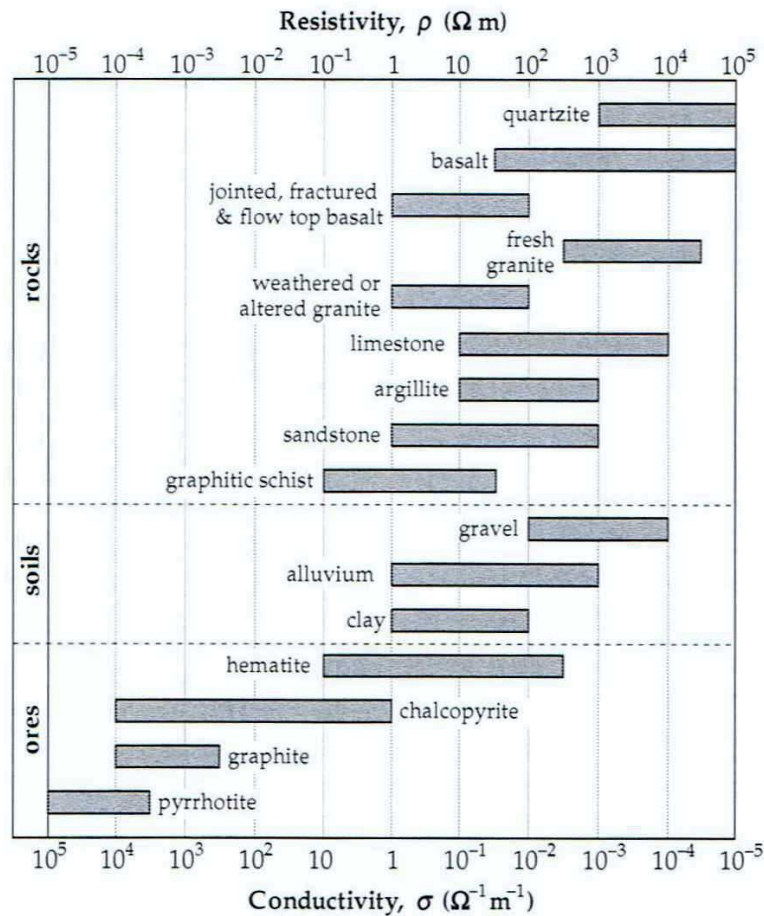
Figure 2-1: Conductivities and resistivities of common rocks, soils and ores. From [Lowrie, 2007]

different rock types can be challenging, because the ranges of the surveyed property, e.g. resistivity, can overlap for different rock types. An overview of resistivities ρ and conductivities σ of common rocks, soils and ores is given in Figure 2-1. Furthermore, the resistivity of porous sediments and sedimentary rocks can vary significantly due to the porosity and the filling of pores. Because there are no unique resistivities for certain rocks, additional information from other survey methods are helpful for identifying different rock units [Lowrie, 2007].

2-1-2 Geoelectric surveys and electrical resistivity tomography

For a better understanding about geoelectrical surveys, the principles of the physics behind need to be clear. Most surveys investigate how resistive or conductive the subsurface is. So, the resistance R can be determined by the current I and the voltage U with the aid of Ohm's law [Lowrie, 2007]

$$U = RI. \tag{2-1}$$

But the resistance is an extensive property and therefore not material characteristic. The intensive counterpart to the resistance is the resistivity ρ. Their relationship can be expressed

as [Lowrie, 2007]

$$R = \rho \frac{l}{A}, \tag{2-2}$$

where l denotes the length of the material sample and A represents its cross-sectional area. So, the resistivity is a material property and therefore more interesting for geophysical surveys, because it allows compared to the resistance the identification of various rock units. The conductivity σ is the reciprocal of the resistivity and is therefore expressed as $\sigma = 1/\rho$ [Lowrie, 2007].

Geoelectric surveys can either be active or passive. While in the case of active sources, an artificial current is injected into the ground, surveys using natural sources measure potentials of naturally occurring fields. These natural currents, also telluric currents, occur mostly due to electrochemical reactions within the subsurface. But there is no option for controlling the source, which can be strongly time dependent. Hence, interpretations are mostly only qualitative and not quantitative. However, the use of natural currents is inexpensive and fast. Active methods give usually better results, because the source is known and therefore also a quantitative interpretation is possible. Additionally the source is controllable and can be modified to optimize the survey for every specific case. Active sources of direct current measurements usually consist of two current electrodes, which are plugged into the ground. So, the Earth is part of the electric circuit. Commonly, a low-frequency alternating current is used for the source to have a direct current for a few seconds. The use of only direct current can cause accumulations of charges at the two potential electrodes, which leads to false signals. The potential electrodes measure the potential at different locations to give the gradient of the electric field [Lowrie, 2007].

A simple option of geoelectric surveys is performing single measurements at certain locations of interest. But nowadays most surveys use the ERT method. Instead of only four electrodes, an array of electrodes is employed for investigating an area of interest. Commonly even-spaced electrode arrays are utilized, but arbitrary configurations are also possible. This array can be a line for two-dimensional surveys or an areal array for three-dimensional surveys. An abundance of measurements are then performed with various combinations of two current and two potential electrodes. The selection of the four electrodes can be arbitrary, but it is common to use certain configurations of the electrodes. The most common configurations are explained in Section 2-1-3. For obtaining information from different depth levels, measurements with different electrode offset are performed. During the measurements, the flowing current is injected at the current electrodes, while the potential is measured at the potential electrodes. In combination with the known geometry, the apparent resistivities ρ_a can be calculated with the aid of Equation 2-3 [Lowrie, 2007]

$$\rho_a = 2\pi \frac{\Delta\varphi}{I} \left[\left(\frac{1}{r_{AC}} - \frac{1}{r_{CB}} \right) - \left(\frac{1}{r_{AD}} - \frac{1}{r_{DB}} \right) \right]^{-1}. \tag{2-3}$$

$\Delta\varphi$ denotes the measured potential difference, I the current and r the distance between the two electrodes given in its index. The indices A, B, C and D refer to the four electrodes. A and B are the current electrodes, while C and D denote the potential electrodes. Note, the resistivity information from each measurement is gathered along the whole path of the current through the subsurface and not at a single point. Therefore, the calculated resistivity is only apparent. Hence, the measured apparent resistivity is the resistivity of a homogeneous half-space. Note that for the special case of a homogeneous half-space, the apparent resistivity

is the true resistivity. For any other case, the true resistivities can be obtained by performing an inversion, which is described in Section 2-1-4 [Lowrie, 2007].

2-1-3 Common four-electrode configurations

The configuration of the electrodes, which describes the ordering of the four electrodes and their respective distances, can be chosen arbitrarily. But there are some specific configurations, which are commonly used. These are configurations are therefore well known and established. Using these has the advantage of comparability between different measurements. Furthermore, these configurations simplify the calculation of the apparent resistivity in Equation 2-3, because the distances r between the electrodes follow defined schemes.

The most common electrode configurations are namely the Dipole-Dipole, the Wenner and the Schlumberger configuration. They are depicted in Figure 2-2. The Wenner configuration sets $r_{AC} = r_{DB} = a$ and $r_{AD} = r_{BC} = 2a$, where a is an arbitrary distance. Therefore the equation for the apparent resistivity reduces to [Lowrie, 2007]

$$\rho_a = 2\pi a \frac{\Delta\varphi}{I}. \tag{2-4}$$

While this equation becomes quite simple by the Wenner configuration, it is often inconvenient for ERT field work. For example, the extend to larger offsets need to be in certain steps, because every distance needs to be the same a [Telford et al., 1990]. Furthermore, large offsets require long cables, especially between the two current electrodes, because in the Wenner configuration their distance is always larger than the distance between the potential electrodes. The Wenner configuration is compared to the other options more sensitive to lateral variations. This can be optimized when the current electrode offset is chosen so that the current flow is maximal in the depth where the most lateral variations are expected. This makes the Wenner configuraton suitable for steeply dipping interfaces such as dykes [Lowrie, 2007].

The Schlumberger configuration is similar to the Wenner configuration, but it has less restriction to the electrode spacing. Both electrode pairs are required to have a common mid point, but their is no relation between the offset of the current electrodes and the potential electrodes. The distances are $r_{AC} = r_{DB} = \frac{L-a}{2}$ and $r_{AD} = r_{CB} = \frac{L+a}{2}$, where L is the distance between the current electrodes and a is the distance between the potential electrodes. Usually, the current electrode distance is kept much larger than the potential electrode distance ($L \gg a$). The apparent resistivity using the Schlumberger configuration can then be calculated by [Lowrie, 2007]

$$\rho_a = \frac{\pi\Delta\varphi}{4I}\left(\frac{L^2}{a}\right)^2. \tag{2-5}$$

This configuration is often used for vertical electric sounding. It is a method for investigating resistivity variations in depth. Therefore, a common mid point is chosen and severals measurements with different offset of the electrodes are performed [Lowrie, 2007].

In the Dipole-Dipole configuration, the current and the potential electrodes can be separated independently. The distance between the electrodes in both pairs need to be the same. But the distance between the two pairs can be arbitrarily. This enables an abundance of possibilities, which raised the popularity of the configuration for ERT surveys. Here, the equation

(a) Wenner
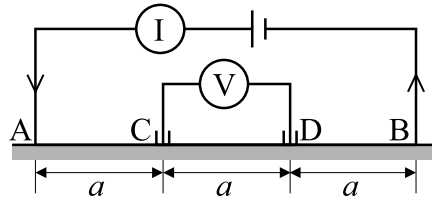
$r_{AC} = a$ $\qquad r_{AD} = 2a$

$r_{CB} = 2a$ $\qquad r_{DB} = a$

$$\rho_a = 2\pi \frac{\Delta V}{I} a$$

(b) Schlumberger
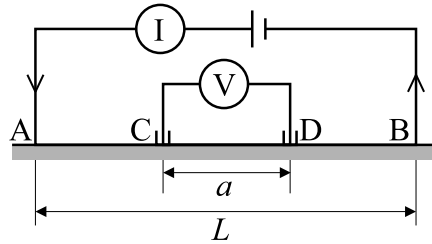
$r_{AC} = (L - a)/2$ $\qquad r_{AD} = r_{CB}$

$r_{CB} = (L + a)/2$ $\qquad r_{DB} = r_{AC}$

$$\rho_a = \frac{\pi}{4} \frac{\Delta V}{I} \frac{(L^2 - a^2)}{a}$$

(c) Dipole-Dipole
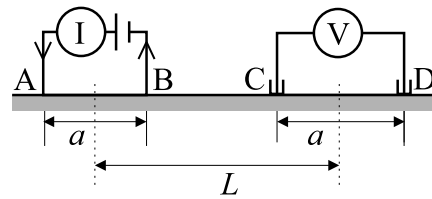
$r_{AC} = L$ $\qquad r_{AD} = L + a$

$r_{CB} = L - a$ $\qquad r_{DB} = L$

$$\rho_a = \pi \frac{\Delta V}{I} \frac{L (L^2 - a^2)}{a^2}$$

Figure 2-2: The different four-electrode configurations. a) Wenner, b) Schlumberger and c) Dipole-Dipole. Note that the potential difference is here denoted as ΔV. After [Lowrie, 2007]

for the apparent resistivity reduces to [Lowrie, 2007]

$$\rho_a = \pi \frac{\Delta \varphi}{I} \left(\frac{L(L^2 - a^2)}{a^2} \right). \tag{2-6}$$

The Dipole-Dipole configuration is advantageous in the field for deep surveys. The electrodes of each pair a comparatively close to each other. Therefore, there is no need for long cables. This enables also surveys with very large offset and therefore greater depth penetration [Burger, 1992].

Note that due to the principle of reciprocity, in all configurations the current and potential electrode pairs can be interchanged arbitrarily [Lowrie, 2007].

2-1-4 Inversion

The ERT measurements give potential differences from which the apparent resistivities can be calculated easily by using Equation 2-3. For obtaining the true resistivities of a heterogeneous subsurface, an inversion of the data is required. The general concept of inversion is to

generate synthetic data from a reference model and to compare it to the observed data. Based on the differences, the reference model is then adapted. This process is repeated iteratively until the reference model can explain the observed data within a predefined error tolerance. The generation of the synthetic data is done by forward modelling. The inversion problem is indeed unique but ill-posed [Günther et al., 2006]. This means in the case of ERT, that there can be multiple resistivity distributions, which result in the same observed data.

A common inversion scheme is the Gauss-Newton scheme. In the following, the model parameters are denoted as $\mathbf{m} = (m_1, m_2, ..., m_M)^T$ with M model cells and represent the resistivities in our model of the subsurface and the data vector $\mathbf{d} = (d_1, d_2, ..., d_N)^T$ with N data points represents the observed apparent resistivities. The data contains errors from the measurement devices and inhomogeneities in the subsurface, which can be used for weighting, if they are available, which is usually not the case. With the aid of an L^2-norm of the weighted residual between the model response $\mathbf{f}(\mathbf{m})$ and the data, the data functional Φ_d have to be minimized. The data functional Φ_d is defined by [Günther et al., 2006]

$$\Phi_d(\mathbf{m}) = \sum_{i=1}^{N} \left| \frac{d_i - f_i(\mathbf{m})}{\epsilon_i} \right|^2 = \left\| diag\left(\frac{1}{\epsilon_i}\right)(\mathbf{d} - \mathbf{f}(\mathbf{m})) \right\|_2^2. \tag{2-7}$$

The errors ϵ can either be measured or have to be estimated.

The minimization problem in Equation 2-7 is highly ill-posed. Therefore, regularization should be applied by installing the model functional Φ_m, which is defined as [Günther et al., 2006]

$$\Phi_m(\mathbf{m}) = ||\mathbf{C}(\mathbf{m} - \mathbf{m}^0)||_2^2. \tag{2-8}$$

Note that $\mathbf{m}^0$ represents the reference model and $\mathbf{C}$ the constraint or smoothness matrix. After to the insertion of Φ_m, the weighted sum with the weighting factor λ needs to be minimized [Günther et al., 2006]

$$\Phi = \Phi_d + \lambda \Phi_m \rightarrow min. \tag{2-9}$$

The weighting factor λ is also known as the regularization parameter. Its choice is a trade-off between data fit and model roughness. The higher the value of λ, the smoother is the model, but also the weaker is the data fit. [Günther et al., 2006]

At this point two options are possible. Either the reference model $\mathbf{m}^0$ contains a priori information and $\mathbf{C}$ is a diagonal weighting matrix, then the model is not altered significantly from $\mathbf{m}^0$. Or $\mathbf{m}^0$ is taken as a constant, while $\mathbf{C}$ handles model characteristics. The latter option means to apply smoothing. Because the problem is underdetermined, the latter option is the method of choice and therefore used in this project [Günther et al., 2006].

In the case of regular meshes, the constraint matrix $\mathbf{C}$ can be taken as a discrete approximation of a partial differential operator of first or second order. If an irregular mesh is used, it is not that straightforward, because also neighbouring relations need to be considered. Therefore, the constraint matrix entries for the tetrahedra i and j with the common face f are $C_{f,i} = -A$ and $C_{f,j} = A$ with A as the face area. In total, the constraint matrix $\mathbf{C} \in R^{B \times M}$ is sparse and contains $2M$ non-zero values. B is the number of faces.

The model vector $\mathbf{m}$ is updated in the manner of [Günther et al., 2006]

$$\mathbf{m}^{k+1} = \mathbf{m}^k + \tau^k \Delta \mathbf{m}^k. \tag{2-10}$$

τ denotes the line search parameter, while k stands for the number of iteration. The line search parameter has to be recalculated in every iteration to avoid overshooting. In the Gauss-Newton scheme of minimizing Φ, Equation 2-10 transforms to [Günther et al., 2006]

$$(\mathbf{J}^T\mathbf{D}^T\mathbf{D}\mathbf{J} + \lambda\mathbf{C}^T\mathbf{C})\Delta\mathbf{m}^k = \mathbf{J}^T\mathbf{D}^T\mathbf{D}(\mathbf{d} - \mathbf{f}(\mathbf{m}^k)) - \lambda\mathbf{C}^T\mathbf{C}(\mathbf{m}^k - \mathbf{m}^0), \qquad (2\text{-}11)$$

with $\mathbf{D}$ being the diagonal matrix $diag(\frac{1}{\epsilon_i})$. Furthermore, $\mathbf{J} \in R^{N \times M}$ denotes the Jacobian or sensitivity matrix. It is given by [Günther et al., 2006]

$$\mathbf{J}_{i,j}(\mathbf{m}^k) = \frac{\partial f_i(\mathbf{m}^k)}{\partial m_j}. \qquad (2\text{-}12)$$

There are several methods for obtaining the sensitivity matrix $\mathbf{J}$ [McGillivray and Oldenburg, 1990]. But the BERT software, which I apply for the inversion in this thesis, uses the formulation [Kemna, 2000]

$$\frac{\partial\varphi}{\partial\sigma} = -\frac{1}{\sigma I}\sum_i\sum_j A_{i,j}\varphi_i^{source}\varphi_j^{receiver}, \qquad (2\text{-}13)$$

which is based on the reciprocity theorem. φ stands for the potential at the source and receiver positions. $\mathbf{A}$ denotes the sparse element matrix. σ is the electrical conductivity or the inverse of the resistivity. Special care needs to be taken to the elements adjacent to the electrodes, because there would an infinite potential occur. These need to be substituted by finite ones for restricting the sensitivity [Günther et al., 2006].

The described calculation needs to be done in every iteration. To reduce the computational effort, the solution of Equation 2-11 can be solved approximately using conjugate gradient techniques [Günther et al., 2006].

The forward operator $\mathbf{f}(\mathbf{m})$ from Equations 2-7 and 2-11 needs to be recalculated in every iteration. This done by forward modelling. Several discretization methods can be implemented, but the most common are FD and FE. Here in this thesis, FE will be applied and therefore explained in the next Section 2-2.

2-2   Finite elements method

When solving Partial Differential Equations (PDEs) analytically, several problems are encountered. First, it is very difficult to solve the problem for complex structures. So, it is helpful to divide the domain in smaller subdomains or cells, instead of solving the corresponding Partial Differential Equation (PDE) once for the whole domain. This, furthermore, allows the investigation of local features. Additionally, a large matrix, which size depends on the number of cells, needs to be inverted. This is only possible, if the matrix is symmetrical. But often this is not the case. And even if it is invertible, this process requires an enormous computational effort. These issues can be circumvent by solving such problems numerically instead of analytically. But numerical methods are not capable of determining the exact solution for the PDE, instead they give an approximation to the exact solution.

There exist different numerical techniques, e.g. the FD method, the finite volume (FV) method and the FE method. Numerical methods are necessary for computer-based calculations of PDEs, because computers are not capable of calculating continuous problems.
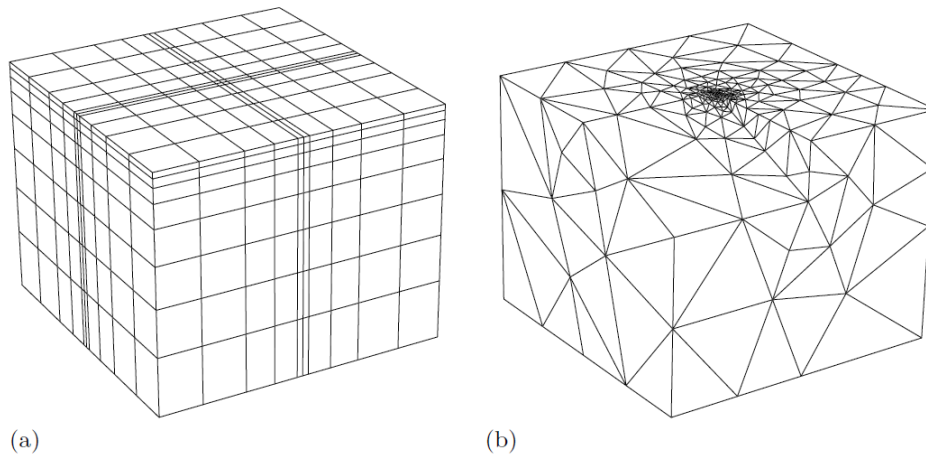
Figure 2-3: Mesh comparison. a) Structured cubic mesh with local refinement. b) Unstructured tetrahedral mesh with local refinement. After [Rücker et al., 2006]

Hence, numerical discretizations are necessary. For this project, the FE method is applied, because it is naturally capable of handling complex geometries [Rücker et al., 2006]. The FE method can be applied in various ways. A common FE technique is the Galerkin method, which I will describe exemplary in the following.

The first step in the FE discretization is the meshing. The design of the mesh, which is used for the computation, is important. The number of nodes defines the spatial resolution and has therefore an significant impact on the accuracy. Furthermore, the number of nodes has a large contribution on the degrees of freedom, which determine the computational effort. For every node an equation needs to be solved. So, the more nodes are used, the more equations need to be solved. But an increased number of nodes also increases the accuracy. Hence, there is a trade-off between the accuracy and the computational effort in the mesh design.

The simplest mesh has structured quadratic/cubic elements, but they are unable to resolve complex geometries. With quadratic/cubic elements only right angles are realizable and therefore curvatures are very difficult to represent in the model. Furthermore, it can be helpful to refine the mesh at areas of interest to enhance the resolution in important areas, e.g. areas with strong gradients [Rücker et al., 2006]. When using quadratic/cubic meshes a local refinement is not efficient. It needs to be performed on whole rows and columns instead on some chosen elements [Rücker et al., 2006]. Therefore, the number of nodes increases significantly. Compared to quadratic/cubic elements, triangular/tetrahedral elements are more adaptable to complex geometries. This adaptability can be increased even more by the use of unstructured elements, because then arbitrarily angles can be used for representing curvatures. Additionally, the advantage of triangular/tetrahedral elements allows arbitrary local refinement. Due to the arbitrary angles, elements can have varying sizes. Summarizing, the use of unstructured triangular/tetrahedral meshes is advantageous, compared to quadratic/cubic meshes, and therefore they will be used in all meshes used in this project. For illustration, the comparison of a cubic and a tetrahedral mesh is given in Figure 2-3.

Additionally, the position of the grid points, the so-called nodes, need to be defined. The simplest option would be to set a node at each angle of the elements. But it is also possible to employ more nodes, e.g. at the center of the element edges or in the center of the element

itself. Various combinations are imaginable. If multiple variables are computed, e.g. velocity and pressure for transport problems, it is possible to allocate certain nodes to a certain variable. But note, that the choice of number of nodes and their position has an impact on the stability of the outcome [Donea and Huerta, 2003].

The PDE that needs to be solved for the ERT problem is [Rücker et al., 2006]

$$\nabla \cdot \left(\frac{1}{\rho} \nabla u \right) \quad = \quad -\nabla \cdot \mathbf{j} \qquad in \, \Omega \subset \mathbb{R}^3, \tag{2-14}$$

with the boundary condition [Rücker et al., 2006]

$$\frac{1}{\rho} \left(\frac{\partial u}{\partial n} + \alpha u \right) \quad = \quad \mathbf{j} \cdot \mathbf{n} \qquad on \, \Gamma. \tag{2-15}$$

Note that Ω is the domain, while Γ represents the boundary. u is the variable that is solved for, so in this case the electric potential and $\mathbf{j}$ is the source current density. The $\mathbf{n}$ is the normal vector, which outwards directed on the corresponding boundary.

For solving the PDE in Equations 2-14 and 2-15 with the FE method, it needs to be transformed into the integral or weak formulation. This is done by multiplying the PDE with the test function v and by integration over the domain Ω [Donea and Huerta, 2003]. The transformed PDE is given by [Rücker et al., 2006]

$$\int_\Omega \frac{1}{\rho} \cdot \nabla v \nabla u \, d\Omega + \int_\Gamma \frac{1}{\rho} \alpha v u \, d\Gamma \quad = \quad \int_\Omega v I \delta(\mathbf{r} - \mathbf{r}_s) \, d\Omega + \int_\Gamma v \mathbf{j} \cdot \mathbf{n} \, d\Gamma. \tag{2-16}$$

In Equation 2-16, v represents the test function, I denotes the source current and δ is the Dirac delta function with $\mathbf{r}$ being the current position and $\mathbf{r}_s$ the source position.

The integrals are hindering, because solving them analytically is very inefficient. Thus, they can be approximated with the aid of the Gauss quadrature integration. It approximates the integrals with a weighted sum (see Equation 2-17) [Schwarz and Köckler, 2011]. The Gauss quadrature integration works more efficient, when applied to a reference element using the coordinates (ξ, κ, ζ). The reference element needs to have the same geometrical body as the physical elements, i.e. for a tetrahedral element, the reference element is also a tetrahedron [de Orio, 2001]. An illustration of a physical element and its corresponding reference element is depicted in Figure 2-4. Now, the Gauss quadrature integration transforms integrals of the FE formulation in the sense of [Bellman and Casti, 1971]

$$\int_{-1}^{1} f(\xi) \, d\xi \quad \approx \quad \sum_{i=1}^{n_{quad}} w_i f(\xi_i). \tag{2-17}$$

Note that n_{quad} denotes the number of quadrature points and w the weighting factors. Equation 2-17 is valid for the 1D case, but can be extended easily to the 2D or 3D case. The quadrature points are interpolated points within the reference element, which are required for the Gauss quadrature integration. The number, position and weighting w_i of the quadrature points depends on the type of element.

Furthermore, the basis or shape functions need to be defined. They interpolate the solution within the discrete nodes defined in the meshing process [de Orio, 2001]. Hence, with their
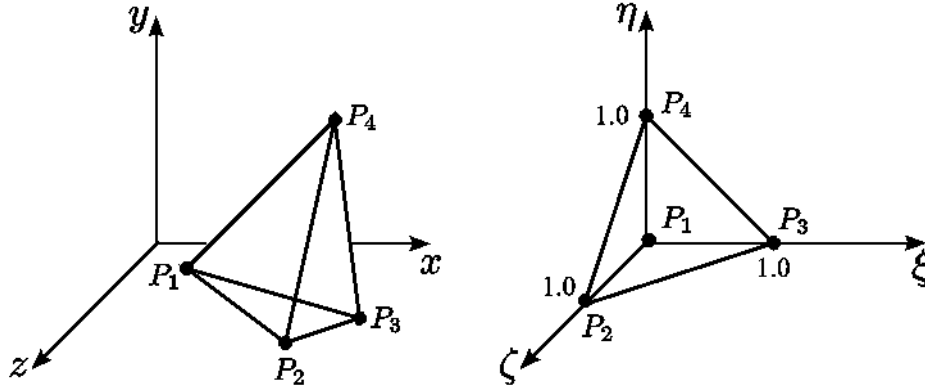
Figure 2-4: Tetrahedral finite element. Left the physical element in the original coordinate
system. Right the reference element in the reference coordinate system. From
[de Orio, 2001]

aid a solution at every point within an element can be obtained. It is also advisable to define
them on the reference element instead of the physical element. The basis functions N are
typically chosen as low order polynomial functions, e.g. [de Orio, 2001]

$$N_i(\xi, \kappa, \zeta) \quad = \quad a_i + b_i\xi + c_i\kappa + d_i\zeta. \tag{2-18}$$

The next step is to transform the reference coordinates to the physical coordinates (x, y, z).
When this is done, the approximate solution u_δ can then be expressed with the aid of the
basis functions [Donea and Huerta, 2003]

$$u_\delta(\mathbf{x}) \quad = \quad \sum_{A\in\nu\backslash\nu_D} N_A(\mathbf{x})u_A + \sum_{A\in\nu_D} N_A(\mathbf{x})u_D(\mathbf{x}_A), \tag{2-19}$$

A denotes the node number, while the index D denotes the values corresponding to a Dirichlet
boundary. The notation $\nu\backslash\nu_D$ represents the all nodes excluding boundary nodes and ν_D all
nodes on the boundary [Donea and Huerta, 2003]. When combining Equation 2-19 with the
PDE a system of equations is obtained for each element. The systems of equations of each
element can be assembled to a global system of equations for the whole domain. This resulting
system of equations is [Donea and Huerta, 2003]

$$\mathbf{Au} \quad = \quad \mathbf{f}, \tag{2-20}$$

where $\mathbf{A}$ is called the stiffness matrix and $\mathbf{f}$ the load vector. The solution is contained in the
$\mathbf{u}$ vector. The system of equations then needs to be solved for $\mathbf{u}$ to obtain the solution.

2-3   Reduced basis method

For cases where a problem needs to be solved multiple times, solving the full problem every
time can be very time consuming. Therefore, a method, which is able to lower the dimension-
ality of the problem, while keeping its accuracy on an appropriate level, is needed. A suitable

technique is the RB method. Such problems are, for example, uncertainty quantifications, where the uncertainties of input parameters are characterized, propagated forward through the model and assessed statistically. Another common application of the RB method is the real time processing of experimental measured data.

In the following Section 2-3-1 the concept of the RB method is pointed out. The technique is split into two stages: The offline and the online stage. In the offline stage the reduced basis space is generated for the particular problem. It is an expensive computation, but has to be performed only once. A detailed description of the offline stage is given in Section 2-3-2. During the online stage, which is explained in Section 2-3-3 the problem is solved multiple times using the previously generated reduced basis space. The calculation of a single solution in the online stage is then usually faster than using FE. Due to the expensive offline stage, the RB method is only reducing the computational effort, if many solutions are needed.

2-3-1   Principles of the reduced basis method

The main interest is to find the exact solution $u(\mu) \in \mathbb{V}$ such that [Hesthaven et al., 2016]

$$a(u(\mu), v; \mu) \quad = \quad f(v, \mu), \quad \forall v \in \mathbb{V}. \tag{2-21}$$

Note that μ denotes the parameter that is varied, while v is the test function. $a(u(\mu), v; \mu)$ and $f(v, \mu)$ are the bilinear forms of the stiffness matrix A and the load vector f. But the exact solution is often mathematically impossible to obtain or requires an extreme computational effort. Thus, it is approximated by seeking the approximated solution [Hesthaven et al., 2016]

$$a(u_\delta(\mu), v_\delta; \mu) \quad = \quad f(v_\delta, \mu), \quad \forall v_\delta \in \mathbb{V}_\delta, \tag{2-22}$$

Properties with the index δ are related to the approximation, in the project the FE approximation. To simplify, it is assumed that the FE approximated solution $u_\delta(\mu)$ converges to the exact solution $u(\mu)$ within a defined tolerance for any parameter $\mu \in \mathbb{P}$ with $\mathbb{P}$ being the parameter space. Therefore, the approximate solution can also be called the truth solution. Another assumption is that a low number of adequately selected basis functions is able to represent the truth solution well [Hesthaven et al., 2016]. Furthermore, it is assumed that the reduced basis space is a subset of the truth solution space. This also implies that $N_{rb} \ll N_\delta$, with N_δ as the dimension of the truth space $\mathbb{V}_\delta$ and N_{rb} as the dimension of the reduced basis space $\mathbb{V}_{rb}$.

The reduced basis problem is then stated as [Hesthaven et al., 2016]

$$a(u_{rb}(\mu), v_{rb}; \mu) = f(v_{rb}, \mu), \quad \forall v_{rb} \in \mathbb{V}_{rb}. \tag{2-23}$$

Note, that all properties denoted with the index rb correspond to the RB method.

For a proper implementation of the RB method, the PDE needs to be separated in a parameter-dependent and a parameter-independent part following the affine decomposition. Thus, the forms $a(\cdot, \cdot; \mu)$, $f(\cdot; \mu)$ and $l(\cdot; \mu)$ need to be decomposed in the manner of [Hesthaven et al., 2016]

$$a(w, v; \mu) \quad = \quad \sum_{q=1}^{Q_a} \theta_a^q(\mu) a_q(w, v), \tag{2-24}$$

$$f(v;\mu) \quad = \quad \sum_{q=1}^{Q_f} \theta_f^q(\mu) f_q(v), \tag{2-25}$$

$$l(v;\mu) \quad = \quad \sum_{q=1}^{Q_l} \theta_l^q(\mu) l_q(v). \tag{2-26}$$

Note, that the l denotes the output functional. The forms a_q, f_q and l_q are independent of the parameter μ and the coefficients θ_a, θ_f and θ_l depend on μ, but are independent of w and v. Because the forms $a_q(\cdot,\cdot)$ do not depend on the parameter, a set of Q_a $N_{rb} \times N_{rb}$-dimensional matrices $\mathbf{A}_{rb}^q$ can already be precomputed after the generation of the reduced basis space in the offline stage. This allows usually a faster computation of $\mathbf{A}_{rb}^\mu$ by [Hesthaven et al., 2016]

$$\mathbf{A}_{rb}^\mu \quad = \quad \sum_{q=1}^{Q_a} \theta_a^q(\mu) \mathbf{A}_{rb}^q. \tag{2-27}$$

The calculation of $\mathbf{A}_{rb}^\mu$ in that manner is independent of N_δ. The linear forms $f(\cdot,\mu)$ and $l(\cdot,\mu)$ are treated in a similar way.

If the affine decomposition is not applicable, the technique of *empirical interpolation* can help to determine an approximate form, which is suitable for the affine decomposition. For more information see [Hesthaven et al., 2016].

Furthermore, it is important to note that the RB method does not depend on a certain discretization method. Hence, it can be applied for example to the FD, FV or the FE method.

Now, that the general concept of the RB method is discussed, the question of accuracy arises. Since the RB method approximates only the numerical approximation, the following triangle inequality holds [Hesthaven et al., 2016]

$$||u(\mu) - u_{rb}(\mu)||_{\mathbb{V}} \quad \leq \quad ||u(\mu) - u_\delta(\mu)||_{\mathbb{V}} + ||u_\delta(\mu) - u_{rb}(\mu)||_{\mathbb{V}}. \tag{2-28}$$

Above, it is assumed that the truth solution u_δ converges to the exact solution u with an appropriate accuracy. Therefore, the accuracy of the RB method depends mainly on the second term on the right hand side of Equation 2-28. Note, that the RB method gives not the same efficiency increase for every problem. While some PDEs work well with the technique, others are unsuitable and have no efficiency increase or, even worse, a loss of efficiency. The method is most suitable for parameterized PDEs, which contain one or more parameters that can be separated in a parameter-dependent and parameter-independent part. For further investigation of the compatibility of a PDE with the RB method, there exists the Kolmogorov N-width. For more details on this, find more information on [Hesthaven et al., 2016].

In the following, the focus turns to the two stages of the RB method: At first the offline stage (see Section 2-3-2), followed by the online stage (see Section 2-3-3).

2-3-2   Offline stage

In the offline stage the reduced basis space $\mathbb{V}_{rb}$ is generated, which is supposed to have a dimension as small as possible, but large enough to approximate the FE solution within

```
Algorithm: The greedy algorithm

Input:       tol, μ₁ and n = 1.

Output:      A reduced basis space 𝕍_rb.
```

1. Compute $u_\delta(\mu_n)$ solution to (3.1) for μ_n and set $\mathbb{V}_{\mathrm{rb}} = \mathrm{span}\{u_\delta(\mu_1), \ldots, u_\delta(\mu_n)\}$

2. For each $\mu \in \mathbb{P}_h$
   a. Compute the reduced basis approximation $u_{\mathrm{rb}}(\mu) \in \mathbb{V}_{\mathrm{rb}}$ defined by (3.3) for μ

   b. Evaluate the error estimator $\eta(\mu)$

3. Choose $\mu_{n+1} = \arg\max_{\mu \in \mathbb{P}_h} \eta(\mu)$

4. If $\eta(\mu_{n+1}) > $ **tol**, then set $n := n + 1$ and **go to 1.**, otherwise **terminate**.

Figure 2-5: Schematic process of the Greedy algorithm, which generates the reduced basis space $\mathbb{V}_{rb}$. u_δ represents the truth solution and u_{rb} the reduced basis solution. *tol* denotes the user defined tolerance and $\mathbb{P}_h$ the discrete parameter space and the parameters itself are denoted as μ. Furthermore, η represents the error between the RB and FE solution. Additionally n is the iteration number. From [Hesthaven et al., 2016]

a certain tolerance. If it is chosen too small, the results have unacceptable uncertainties. If it is chosen too large, the computation becomes inefficient. The reduced basis space is generated by the Greedy algorithm or Greedy basis generation. Its scheme is depicted in Figure 2-5. It is an iterative process, where in each iteration one basis function is added, which increases the precision of the set of basis functions. In each iteration one truth solution has to be computed to generate the corresponding basis function. An essential component of the Greedy algorithm is the estimation of the error $\eta(\mu)$ to determine how the precision of the solution has changed by replacing the FE approximation space $\mathbb{V}_\delta$ by the reduced basis space $\mathbb{V}_{rb}$. The error is estimated, because determining the actual error is often linked with a high computational effort. Hence, an estimation of the error is usually advantageous [Hesthaven et al., 2016]. Since the RB method is also used in real-time applications, where verifications are often neglected for saving computational resources, the estimation of the error needs to be fast and reliable. The results of the approximation, using error estimations, have often an appropriate accuracy, because the estimators use usually large training sets with a fine sampling of parameters. Hence, the error is based on the discrete set of parameters $\mathbb{P}_h$ instead of the continuous parameter space $\mathbb{P}$ [Hesthaven et al., 2016].

There are various ways to estimate the error. In the utilized software package *DwarfElephant* (for more information see Section 3-3-3) the relative output bound is used. Therefore, it is also used for the simulations in this project. The relative output bound $\eta_{s,rel}$ is defined as [Hesthaven et al., 2016]

$$\eta_{s,rel}(\mu) \quad = \quad \frac{||\hat{r}_\delta(\mu)||_{\mathbb{V}}^2}{\alpha_{LB}(\mu)\, s_{rb}(\mu)}. \tag{2-29}$$

Note that α_{LB} represents the lower coercivity bound and $\hat{r}_\delta$ denotes the Riesz representation of $r(v_\delta; \mu) = f(v_\delta; \mu) - a(u_{rb}(\mu), v_\delta; \mu)$. Furthermore, s_{rb} stands for the output [Hesthaven et al., 2016]. This error estimator is the rigorous upper bound of the output of interest. For a mathematical derivation of the error estimator and for alternative options beside the relative output bound, see [Hesthaven et al., 2016]. With the aid of the error bound, the resulting error from every iteration of the greedy algorithm can be evaluated and

the number of basis functions can be chosen properly.

In the course of the iterative basis selection, for the case that there is at the n-th iteration step an n-dimensional reduced basis space $\mathbb{V}_{rb}$, the estimated model order reduction error is maximized by the next basis function $u_{rb}(\mu_{n+1})$. Therefore, [Hesthaven et al., 2016]

$$\mu_{n+1} \quad = \quad \arg\max_{\mu \in \mathbb{P}} \eta(\mu). \tag{2-30}$$

Then, $u_\delta(\mu_{n+1})$ is calculated to extend the reduced basis space $\mathbb{V}_{rb} = span\{u_\delta(\mu_1),...,u_\delta(\mu_{n+1})\}$. Hence, the neglected basis function with the largest impact on the solution will be included in the reduced basis space $\mathbb{V}_{rb}$. This procedure is continued in a loop until the maximal estimated error falls below a predefined error tolerance. Thus, the algorithm picks the next sample point, where the estimated error $\eta(\mu)$ is maximal. Hence, the reduced basis tries to be optimal in the maximum norm over $\mathbb{P}$ [Hesthaven et al., 2016]. Note that for the case of insufficient accuracy of an N_{rb}-dimensional reduced basis space, it can be extended by n more modes, which has the same result as generating it initially with $N_{rb} + n$ basis functions.

The computational effort of the offline stage is dominated by the necessary step of solving the truth problem N_{rb} times [Hesthaven et al., 2016]. But so far no actual solution is obtained. This is done in the online stage, which is outlined in the following section.

2-3-3   Online stage

Now that the reduced basis space $\mathbb{V}_{rb}$ is defined, the procedure can move on to the online stage of the RB method. In the case of an ideal setting, the computational effort would be independent of the dimension of the truth solution space N_δ. It would only depend on the number of basis functions N_{rb} ($N_{rb} \ll N_\delta$) [Hesthaven et al., 2016].

Actually, for each calculation with a different parameter the reduced basis solution matrix $\mathbf{A}_{rb}^\mu$ would need to be recalculated. Because the parameter μ can be contained in the bilinear form $a(\cdot, \cdot; \mu)$, the recalculation would require the construction of the truth matrix $\mathbf{A}_\delta^\mu$. This would have the issue that $\mathbf{A}_\delta^\mu$ depends on N_δ. But the N_δ-dependent computation can be circumvent by assuming that the PDE can be separated in a parameter-dependent and a parameter-independent part according to the affine decomposition described in Section 2-3-1. The computational effort of the online stage depends mainly on N_{rb} instead of N_δ. Since $N_{rb} \ll N_\delta$, this is usually more efficient than computing the truth solution for every parameter value [Hesthaven et al., 2016]. From a more practical point of view, in the online stage one can compute various solutions at a reduced cost, since the basis space generation is already precomputed in the offline stage and this basis space just needs to be combined with the parameter dependent part of the PDE [Hesthaven et al., 2016].

If only one solution is required, the RB method is much more inefficient than standard methods like the FE method, because the basis space generation in the offline stage is very expensive. But when the basis space is generated, the computation of a single solution is much faster. Hence, the RB method becomes more and more efficient, the more solutions need to be calculated [Hesthaven et al., 2016].

2-4   Uncertainty Quantification

Uncertainties are a common issue in surveys and simulations. To obtain a better understanding of the reliability of the data, an uncertainty quantification is a helpful tool. It characterizes the input uncertainties and forward propagates them through the computational model. Furthermore, statistical or interval assessments can be performed on the resulting responses [Adams et al., 2014].

There exist several ways of performing an uncertainty quantification. One way is the Bayesian calibration, where the uncertain parameters are characterized by probability density functions. These probability density functions describe the permissible parameter values. It then incorporates data to estimate with the likelihood function how well the model and its parameters describe the data [Adams et al., 2014]. The specific likelihood function used in software in this thesis is based on Gaussian probability density functions [Adams et al., 2014].

A common method of the Bayesian calibration is the MCMC method. It estimates the expectation of a function with respect to a distribution. It bases on a Markov chain, where a random walker explores the search space and successively visits solutions with stable frequencies originating from the distribution. After a burn-in phase, the Markov chain allows the walker to reach a stationary regime [Vrugt et al., 2009].

For the process of the walk through the search space, the MCMC algorithm performs trial moves from the current position of the Markov chain $\mathbf{x}_{t-1}$ to a new state $\mathbf{z}$. The candidate location $\mathbf{z}$ is sampled from a proposal distribution, which depends on the current location. The candidate location is then tested by the Metropolis acceptance probability, which either accepts or rejects the candidate location. If it is accepted, it becomes the new current location and the Markov chain moves on to $\mathbf{z}$. Otherwise, the Markov chain stays at the current location $\mathbf{x}_{t-1}$ and a new candidate location is tested. After multiple iterations, the MCMC algorithm will reach a stationary regime, if existing for the particular problem, and stop [Vrugt et al., 2009].

The classical MCMC algorithm has the issue, that it often requires a lot of iterations to reach the stationary regime. Therefore, an alternative scheme evolved to reduce the required computational effort: The DREAM scheme [Vrugt et al., 2009]. It estimates a distribution of crossover probabilities that prefers large jumps over smaller ones in every chain. Hence, the stationary regime is reached faster [Vrugt et al., 2009]. Furthermore, outlier chains can occur that deteriorate the performance. In the DREAM algorithm, these outlier chains are removed [Vrugt et al., 2009]. Additionally, the DREAM scheme uses a decreasing step size. Thus, at the beginning of the algorithm large steps are performed to approach the stationary regime and later the steps are smaller to reach the stationary regime properly without overshooting it [Vrugt et al., 2009].

For this research project, the DREAM algorithm is used.

<div style="text-align: right">

Chapter 3

Methods

</div>

For giving more comprehensible insights in how the results given in Chapter 4 are obtained, the general workflow (see Section 3-1) and a short description of the utilized software (see Section 3-3) is presented in this chapter.

3-1 General workflow

For getting an idea of how the results in the Chapter 4 are obtained, the general workflow will be presented here. The workflow is illustrated in Figure 3-1.

The first step is to a generate synthetic data sets on the base of a simple predefined model. This model is designed in the software package BERT ([Rücker et al., 2006], [Günther et al., 2006]), which is described in Section 3-3-1. For the calculation, a mesh is required. Therefore, BERT utilizes the tool *Tetgen* [Si, 2003]. The next step is to perform a forward simulation on the generated mesh to obtain the synthetic data set. This process is also done using the software BERT. To do so, the electrode and measurement configuration has to be defined. The forward simulation gives then for every single measurement the resulting potential difference and calculates the corresponding apparent resistivity. Furthermore, noise is added. Since the synthetic data are used as a surrogate for measured data, the noise is important to let the synthetic data appear more as measured data. The inversion is also performed by the software package BERT. The idea of this back-and-forth process is to induce uncertainty. The theory behind the inversion is described in the theory part in Section 2-1-4.

On the base of the inversion result, a new model is built using *Gmsh* [Geuzaine and Remacle, 2009]. These rebuilt models are then used in the next step to perform forward simulations with the FE and RB method. Therefore, I use the software package *DwarfElephant*, which bases on the simulation environment *MOOSE* [Gaston et al., 2009]. Both are described in Section 3-3-3. The forward simulations of the FE and RB method are supposed to give the same result within a defined tolerance.

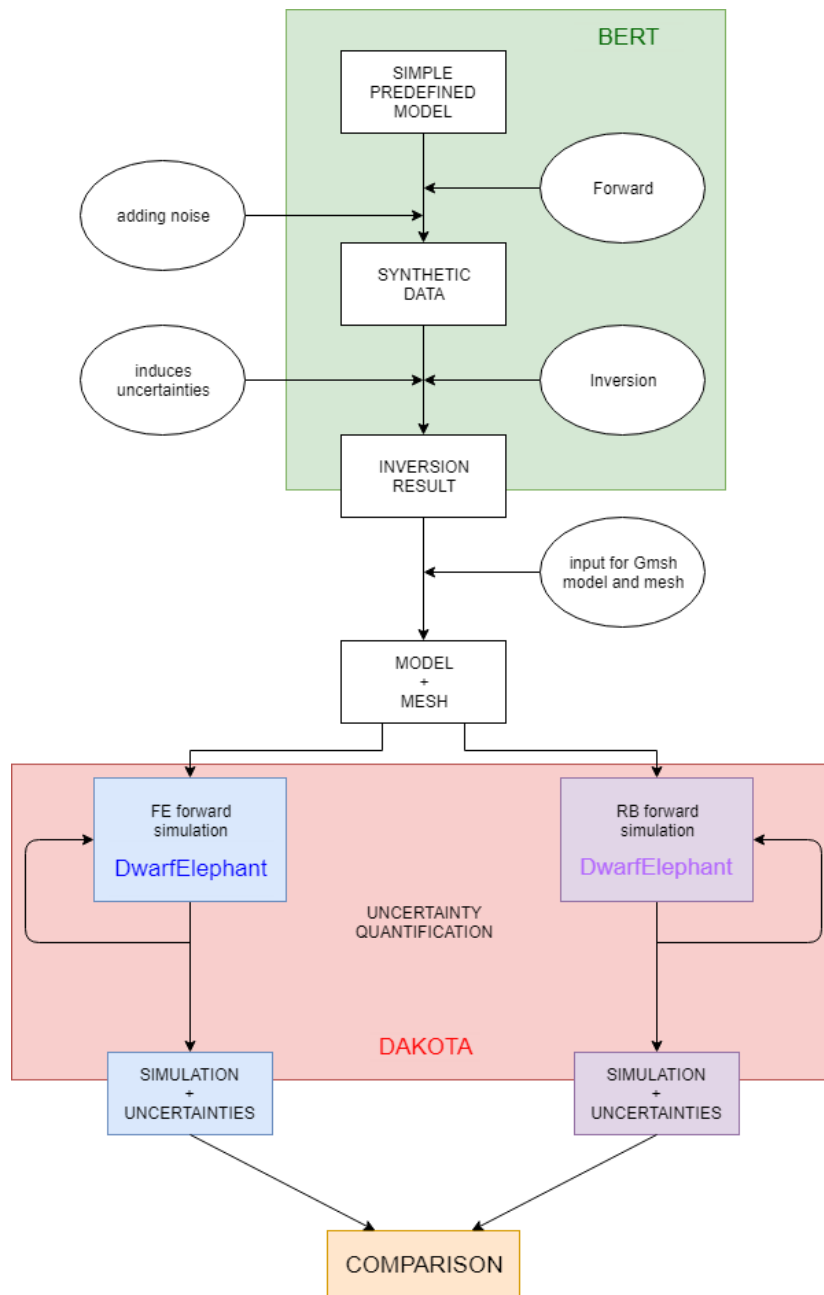For comparing these data sets with the data set of the BERT forward simulation, a *Python*

Figure 3-1: Schematic illustration of the workflow of the research project.
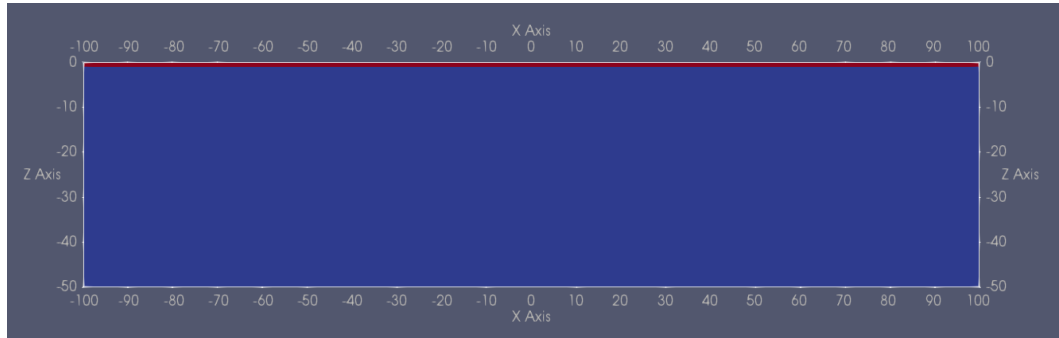
Figure 3-2: A two layer case used as the initial model. The upper layer is shown in red, while the lower halfspace is colored in blue. The background is indicated in grey.

script is used to perform multiple simulations by calling *DwarfElephant*. Each simulation is performed with a different source position. When all simulations are done, the potential differences of each measurement is calculated and assembled the same way as in the BERT data set. The actual comparison of the data sets is supposed to be done in an uncertainty quantification. Unfortunately, this could not be done, due to a lack of time. Therefore, the software package *Dakota* [Adams et al., 2014] is utilized, which calls the *Python* script to simulate the ERT data set. The uncertainty quantification is supposed to be done twice. Once using the FE forward simulation and once using the RB forward simulation. There are two purposes for the uncertainty quantification: On the one hand, the uncertainties induced by the inversion process are supposed to be investigated and on the other hand the computational effort of the FE and the RB method are supposed to be compared in a large computation.

3-2   Model

The initial model, which is used for the inversion, is presented in the following. For the purpose of comparing the performance of FE and RB simulations and investigating the uncertainty induced by the inversion, no special requirements to the model are given. Hence, any model is suitable. Therefore, a very simple two layer case is used. To limit the computing times in the uncertainty quantification, the model is in 2D. The domain has an extend of 200 m in x-direction and a depth of 50 m in z-direction. The upper layer has a thickness of 1 m, while the lower layer is the underlaying halfspace. Both layers themselves are completely homogeneous. The interface between the two layers is horizontal. The geometry of the model is depicted in Figure 3-2.

Furthermore, the resistivities of the layers need to be defined. A resistivity of 10 Ωm is allocated to the upper layer and a resistivity of 100 Ωm is assigned to the lower halfspace. According to Figure 2-1, these values are plausible for geoscientific purposes. The resistivity value of 10 Ωm of the upper layer could possibly represent for example an alluvium or a clay, while the resistivity value of 100 Ωm of the lower halfspace is suitable for example for a limestone or a sandstone.

3-3 Utilized software

In the progress of this research, several software packages are used. In order to make the process more transparent for the reader, the various software packages will be described briefly in the following. At first, the ERT related software BERT is introduced in Section 3-3-1, followed by the meshing software *Gmsh* in Section 3-3-2. The Section 3-3-3 focuses on the simulation framework *MOOSE* with its RB application *DwarfElephant*. Finally, the parametric analysis framework *Dakota* is introduced in Section 3-3-4.

3-3-1 Boundless electrical resistivity tomography

The *Boundless Electrical Resistivity Tomography* software [Rücker et al., 2006][Günther et al., 2006], or abbreviated BERT, focuses mostly on the inversion of direct current electrical measurements, but also allows forward modelling to obtain synthetic data. The used method is 'boundless' because the domain is extended to set the boundaries far from the area of interest to reduce the impact of boundary conditions. The software originated from the *Direct Current Finite Element Method Library*, or short *DCFEMLib* [Rücker et al., 2006], which is based on C++. But over the time, it has been partly replaced by the Python-based *Generalized Inversion and Modelling Library* [Rücker et al., 2017], or short *pyGIMLi*.
The applied inversion scheme is generally based on the smoothness-constraint Gauss-Newton inversion. More details on the inversion scheme can be found in Section 2-1-4. The forward modelling, which is also part of the inversion process, is done using the FE discretization method [Günther et al., 2006].
BERT employs unstructured tetrahedral meshes. This has the advantage over structured cubic meshes that arbitrary geometries can be adapted sufficient and local mesh refinements are more efficient. For the mesh generation, BERT employs the software *TetGen* [Si, 2003]. Compared to other software packages with a similar use, BERT utilizes a triple grid approach instead of a dual grid approach. The parameter mesh is coarse and defines the resolution of the inversion. The secondary field mesh is globally refined and prolonged for the forward calculation. Finally, the primary potentials are computed on the very fine primary field mesh. The triple grid approach, including the secondary field mesh, allows a fast calculation [Günther et al., 2006].

3-3-2 Gmsh

The software *Gmsh* [Geuzaine and Remacle, 2009] is a 3D FE grid generator. The intention of the *Gmsh* is to supply a fast, light and user-friendly meshing tool. It is designed to be fast enough to generate useful meshes for FE calculations on standard personal computers and being light in the sense of required computational resources. Furthermore, the software is intended to be user-friendly by supplying a graphical user interface and having a robust and portable code. It contains a built-in CAD engine and postprocessor. Additionally, *Gmsh* features parametric input and advanced visualization capabilities. The software is completely developed in C++ [Geuzaine and Remacle, 2009]. *Gmsh* is an open-source software and can be obtained from http://www.gmsh.info.

3-3-3 MOOSE Framework & DwarfElephant

The multiphysics object-oriented simulation environment, or short *MOOSE Framework* [Gaston et al., 2009] was coupled with the *Dakota Framework* [Adams et al., 2014]. It is developed by the *Idaho National Laboratory* with the intention to provide a framework for scientist and engineers to develop new simulation applications with low effort. *MOOSE* is based on finite element (FE) method using the continuous or discontinuous Galerkin formulation or the Petrov-Galerkin formulation. Furthermore, unstructured meshes with any dimensionality up to three is supported. The software is free to use and more information can be found on `https://mooseframework.org`.
The software package *DwarfElephant* is an application based on the *MOOSE Framework*. It offers simulations using the reduced basis (RB) method. The application was developed by the *CGRE* Institute of *RWTH Aachen University*. It is free to use and available on Github on `https://github.com/cgre-aachen/DwarfElephant`.

3-3-4 Dakota framework

The *Dakota Framework* [Adams et al., 2014], developed by the *Sandia National Laboratories* in Albuquerque, NW, USA, is a software to perform advanced parametric analyses. It is no simulation software itself, instead it is aiding simulation software with giving additional options to analyse and improve the simulation. Despite containing internal simulation software, the *Dakota Framework* can be coupled with external simulation software. A scheme of the coupling is depicted in Figure 3-3.
 Then a variety of iterative analyses can be performed. The software offers parameter studies and sensitivity analyses, which varies to input parameters to evaluate their impact on the simulation results. Another capability of the *Dakota Framework* are Design of Experiments techniques, which seek to extract trend data from a parameter space using a limited number of sample points. Furthermore, uncertainty quantifications are also part of the software. They forward propagate uncertainties in the input parameters trough the computational model and perform statistical and interval assessments on the responses. Additionally, the *Dakota*
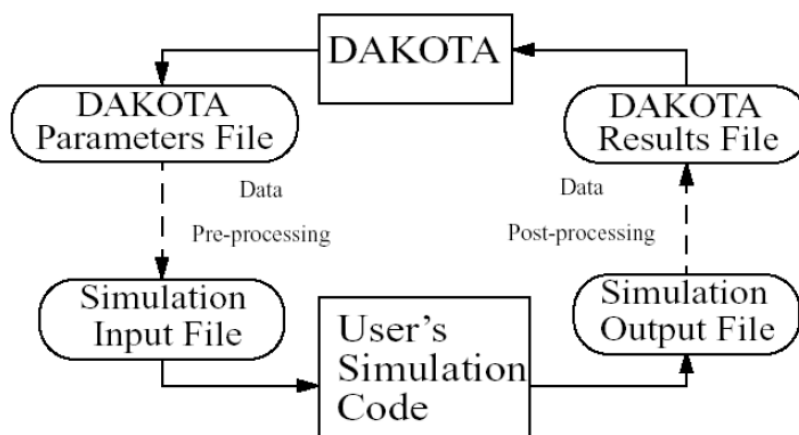

Figure 3-3: Basic scheme of the coupling of the *Dakota Framework* with the user's simulation software. From [Adams et al., 2014].

Framework offers optimization solvers, which are intended to maximize or minimize the objective function calculated by the coupled simulation software to optimize the performance and efficiency of the computation. Moreover, performing a calibration is also a possibility of the software. It is used to maximize the agreement between simulated data and measured or desired data. This is usually helpful for inverse problems. Because such iterative calculations are often consuming a lot of computational resources, the *Dakota Framework* is designed to exploit the capabilities of parallel computing [Adams et al., 2014].

Summarizing, the *Dakota Framework* is created to obtain improved or even optimal experimental designs, to get a better understanding of the sensitivity and uncertainty of a specific problem and to generally to improve the performance of the simulation [Adams et al., 2014]. The *Dakota Framework* is free to use and more information can be found on `https://dakota.sandia.gov`.

Chapter 4

Results

In the following, the results including intermediate results will be presented. In the first Section 4-1, I will describe the generation of the synthetic data and their corresponding inversion results. Afterwards I will give the model, which is generated on the base of the inversion result, followed by the forward simulation using the FE and RB methods in Section 4-2. The next section illustrates the results of the uncertainty quantification (see Section 4-3).

4-1 Inversion results

After generating the model, which is described in Section 3-2, it is forward modelled to obtain synthetic field data with the aid of BERT ([Rücker et al., 2006],[Günther et al., 2006]). Therefore, the position of the electrodes and their measurement configuration need to be defined. 18 electrodes are employed at the surface from x-positions ranging from $0\,m$ to $17\,m$ with an electrode spacing of $1\,m$. The number is electrodes is rather small, but sufficient as the model contains only a feature at a depth of $1\ m$, no deep penetration is required. For the measurements, the dipole-dipole configuration is chosen. The use of the Dipole-Dipole configuration allows more measurements for the same amount of source electrode positions than the Wenner and the Schlumberger configuration. For each source position, one forward simulation is required, since a new source position generates a different electrical field. Therefore, with the Dipole-Dipole configuration, more information can be obtained from a single forward simulation.

The distance between the two electrodes of the source and potential electrode pairs is kept constant of $1\ m$. Thus, the 18 electrodes allow 15 possible source positions without performing reciprocity measurements. For all 15 source positions, all possible measurements are performed. This results in a number of 120 measurements with offsets ranging from $2\ m$ and $16\ m$.

  After the forward simulation an error of 3 % is added to the measured potential differences. This is import, because otherwise the synthetic data would give a perfect representation of the model. But synthetic data are not supposed to be perfect, because they should be surrogates for real data. Hence, the added error represents random noise in real measurements.
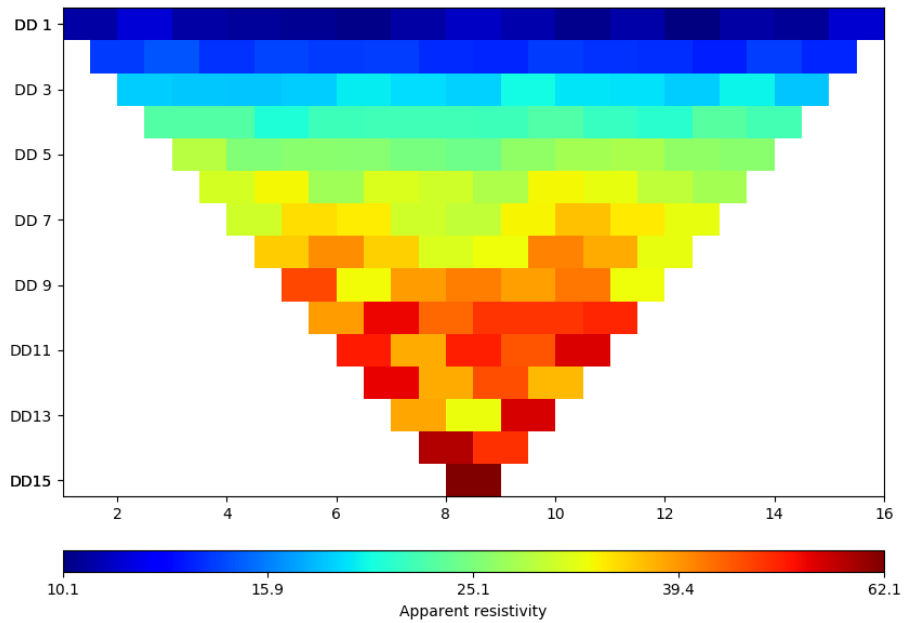
Figure 4-1: Pseudosection of the forward modelled apparent resistivities. Note that the z-axis only shows depth levels and no actual depth.
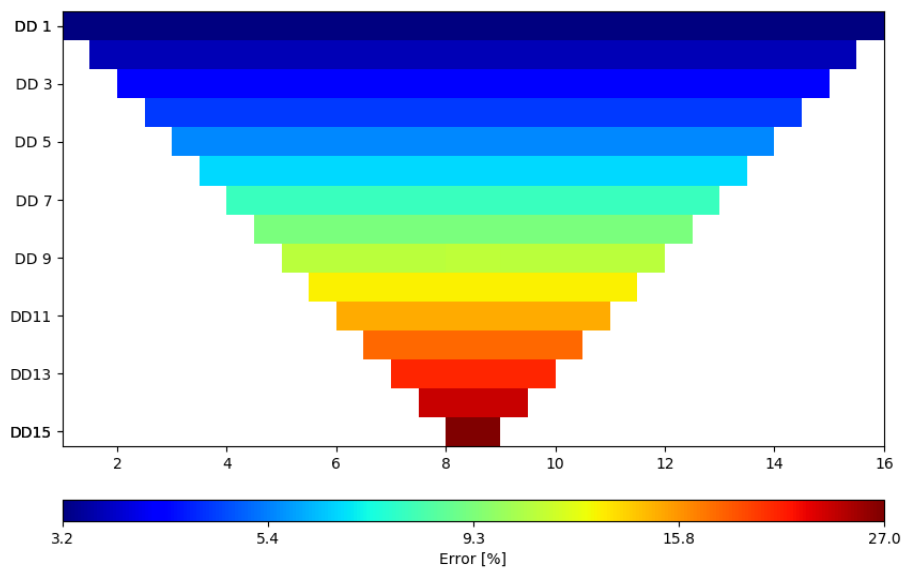

Figure 4-2: Pseudosection of the error in the forward simulation. Note that the z-axis only shows depth levels and no actual depth.
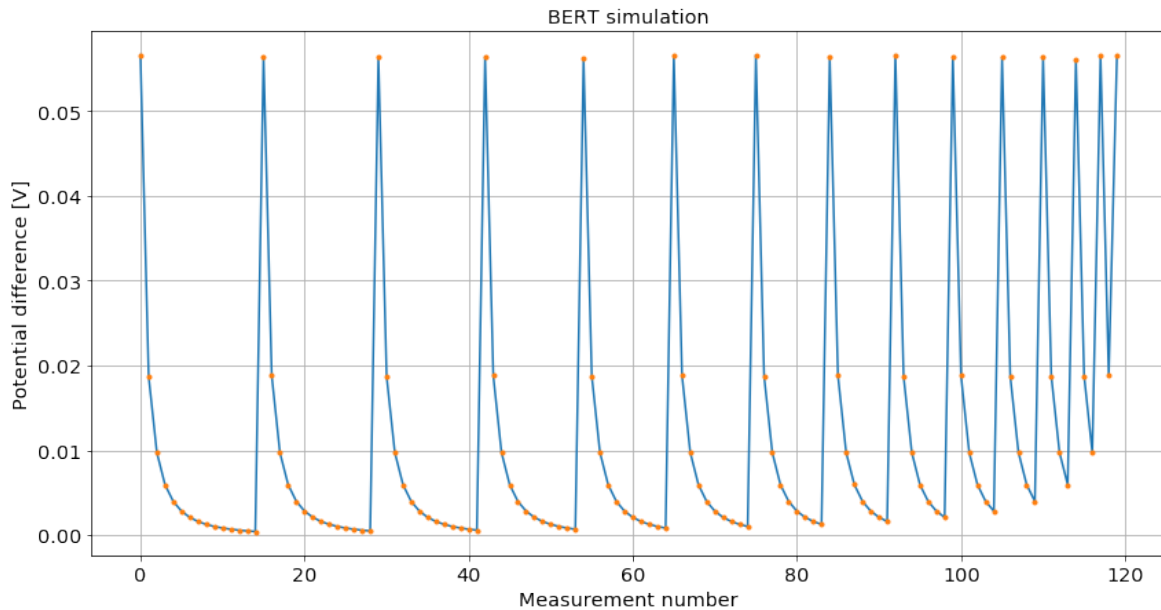
Figure 4-3: Resulting potential differences of the BERT forward simulation. Note that each block represents all measurements with one source position, but varying offsets. Each block starts with a peak.

The resulting pseudosection of the forward modelling is depicted in Figure 4-1. The data are apparent resistivities. The actually modelled data is the potential, but with the potential differences of the potential electrodes the apparent resistivities can be calculated with the aid of Equation 2-6. The apparent resistivity values range from $10.14 \, \Omega m$ to $62.11 \, \Omega m$. Furthermore, a gradient in the apparent resistivities can be observed. In the upper depth levels the smaller values are located, while the larger values are positioned in the lower depth levels. Additionally, the values within the depth levels vary. These variations are small in the upper depth levels and become more significant with depth. This is related to the error of the forward simulations shown in Figure 4-2. The error increases with the geometrical factor and therefore the depth level and so the measurements have more variations and are less reliable. The behaviour of the error depicts reality, because the current needs to penetrate more material and therefore more errors might be induced. The error distribution does not show more other features. For a later comparison of the forward simulation using BERT and the forward simulation using *DwarfElephant*, I will use the measured potential differences. Alternatively, also the apparent resistivity could have been used. But none of these modelled properties gives more information as the other one. The resulting potential differences are depicted in Figure 4-3. Note that each block represents all measurements with varying offsets with one source position. Each block starts with the smallest possible offset and ends with the largest. The block become smaller with increasing measurement number, since the number of measurements per source position decreases to skip reciprocity measurements. The blocks follow a certain structure. Each block is similar to the previous one, but with the last measurement missing. Hence, measurements with same offsets give similar results. I will compare this potential difference data set later with the ones of the FE and RB data sets calculated with *DwarfElephant*. Please note that, in the following, I will distinguish the simulations of *DwarfElephant* by their method, namely FE and RB, and I will call the simulation done in
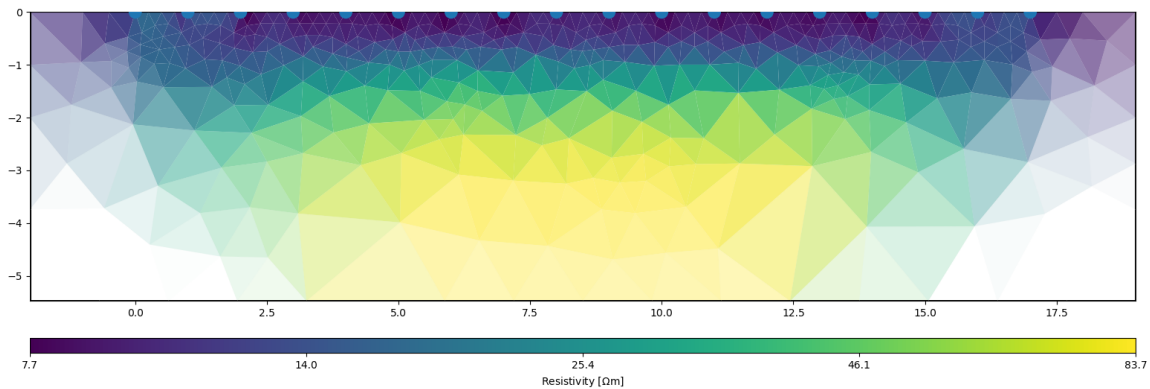
Figure 4-4: Resisitivity distribution as the result of the inversion for the two layer case. The electrode positions are indicated by the blue dots at the surface.
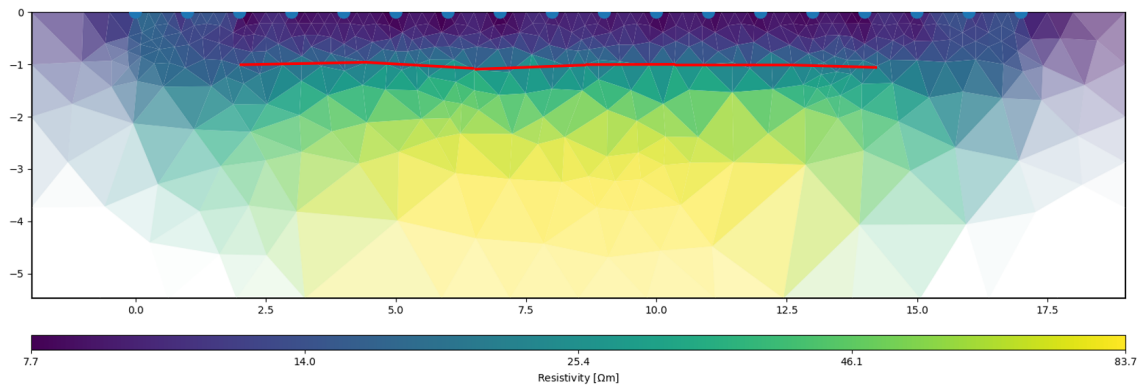

Figure 4-5: Interpreted resistivity distribution. One interface is interpreted an at depth varying from about 0.8 to about $1.2\ m$. Therefore, the interpretation suggests a two layer case.

BERT only BERT simulation, despite that it is a FE simulation too.

In the next step, the synthetic data are inverted. This process is also performed with the BERT software using the inversion scheme described in Section 2-1-4. This back-and-forth calculation is necessary because one of the ideas of this project is to investigate the uncertainty induced by the inversion. The inversion process ends after only two iterations, but the results are sufficient. The process is stopped, because the data fit criteria is reached by the error weighted χ^2 fit drops below 1. Its value is 0.9725. The relative root mean square between the data and the response is 10.264 %. Good values of the relative root mean square would be between $1-2$ % [Günther and Rücker, 2017]. Hence, the value here is not good but acceptable. The result of the inversion is given in Figure 4-4. In the inversion result, the upper area exhibits quite stable values. This area ranges from the surface to a depth varying from about 0.8 m to 1.2 m. The resistivity values in this upper area range from about 7.7 Ω to about 17.3 Ωm. After this depth, the resistivity increases stronger to a value of about 87.8 Ωm at a depth of about 5 m. Due to this change, an interface between two geological layers is interpreted. Hence, the interpreted interface varies from depths of about

0.8 m to 1.2 m. The interpretation is depicted in Figure 4-5. So, the result of the inversion suggests two layers. This correlates with the initial model, which also has two layers with the interface at 1 m. But the interpreted interface is not straight, instead is has variations according to variations in the inversion result. The interpretation is used to build up a new model, which is used for the forward simulations using FE and RB in the software packages *MOOSE* [Gaston et al., 2009] and *DwarfElephant*.

4-2 Forward modelling results

For the forward modelling with the FE and RB method using the software packages *MOOSE* [Gaston et al., 2009] and *DwarfElephant*, a model and a mesh are required. I generated these on the base of the interpretation of the inversion result. The model with the corresponding mesh is displayed in Figure 4-6 and a close-up on the area of interest is depicted in Figure 4-7. For the model, I used the 'boundless' concept of BERT ([Rücker et al., 2006],[Günther et al., 2006]). Hence, the domain is expanded so the boundaries are placed far away from the region of interest with the intention to reduce the impact of the boundary conditions. Therefore, the model domain has a horizontal extent of 200 m and a vertical extent of 50 m. But note that the model is non-dimensionalized to an horizontal extent of 1 and a vertical extent of 0.25. This enhances the performance of the forward simulation, because the values for the calculation have similar magnitudes. The interface in the area of interest originates from the interpretation of the inversion results. But the inversion result gives no information about the depth of the interface at the boundaries. Therefore, I placed the interface at the boundaries to the average depth of the other interface points. The resistivity values of the two layers are obtained by averaging. The resulting resistivity of the upper layer is defined as 11.898 Ωm in the model, while a resistivity of 56.933 Ωm is assigned to the underlying halfspace.

For the mesh unstructured triangular elements are used. The element sizes vary intentionally to increase the resolution in the area of interest and decrease the resolution in less interesting regions. The mesh has 17266 elements and 8634 nodes in total.

Now, that the mesh is generated the forward simulations can be performed. First, I will present the results of the FE simulations. Afterwards I will show the results of the RB simulations.

The ERT problem is a steady state problem, because a direct current is used and therefore, the electrical field is assumed to be constant over time. This can also be observed in the ERT problem formulation in Equations 2-14 and 2-15, which do not contain any time derivatives. The surface is considered as a Neumann boundary condition with a value zero. The air is very resistive and therefore, it is assumed that there is no flow through the surface. To the other boundaries Robin or Mixed boundary conditions are assigned. At these boundaries the electrical field can propagate through the boundaries. This represents that in reality the electrical field propagates into surrounding rocks. Therefore, the Robin boundaries have a stronger Neumann character and their penalty value is set to a small value of 1. Due to the 'boundless' concept, it is assumed that the boundary elements are far away and that their boundary conditions have no significant impact on the electrical field originated from the source. The source and sink at the source electrode pair are set to 0.1 A and -0.1 A respectively. Note that the source and sinks are always positioned to a depth of 0.1 m to avoid an interchange of the source and sink themselves with the Neumann boundary condition
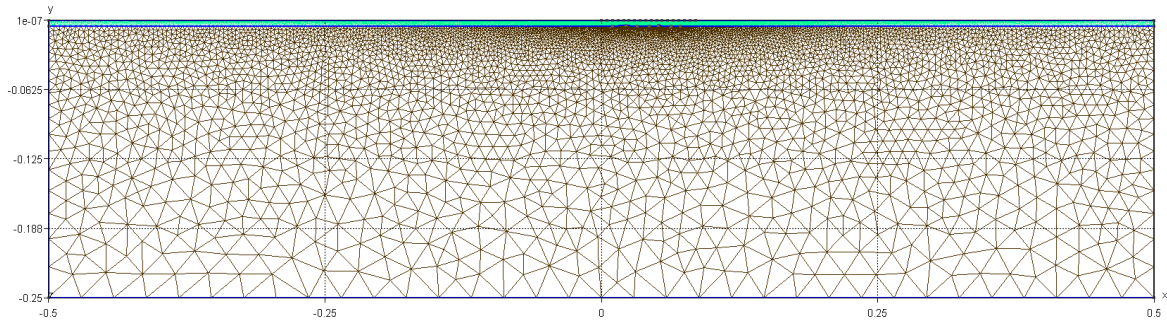
Figure 4-6: Model and mesh based on the inversion result. Note that the domain is expanded following the boundless concept. Furthermore, the element sizes of the mesh vary to increase the resolution in the area of interest. The model and the mesh are generated with the aid of *Gmsh*. Note that the mesh is dimensionless to improve the performance of computations. The physical model would have a horizontal extent of $200\ m$ and a vertical extent of $50\ m$.

Figure 4-7: Close-up of the model and its mesh based on the inversion result. The close-up shows the region of interest, which originates from the interpretation of the inversion, displayed in Figure 4-5.

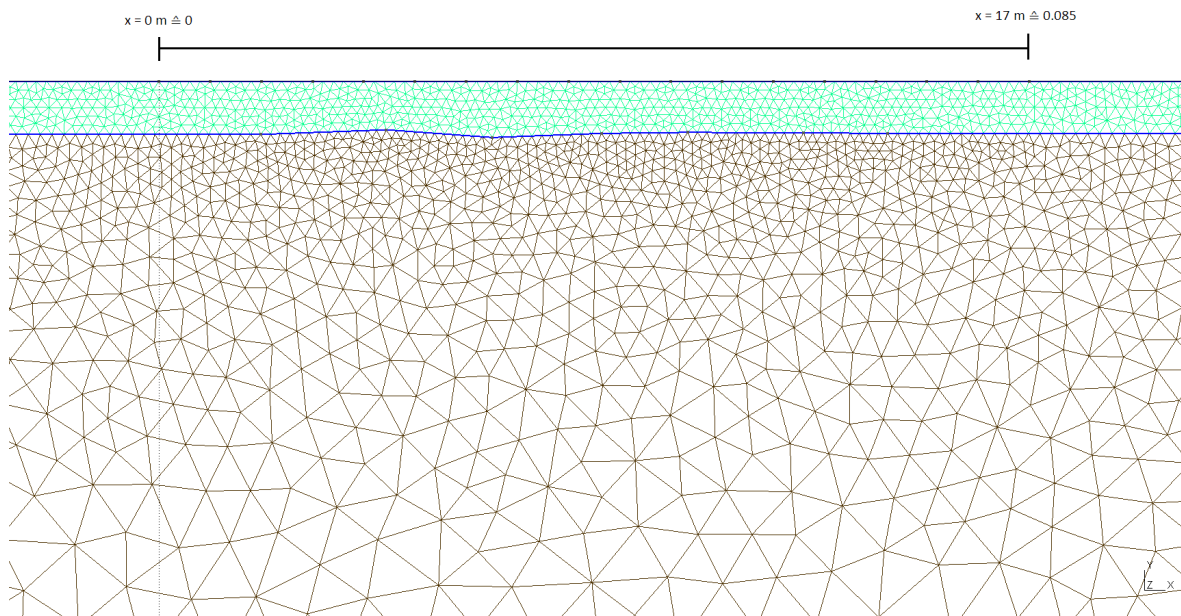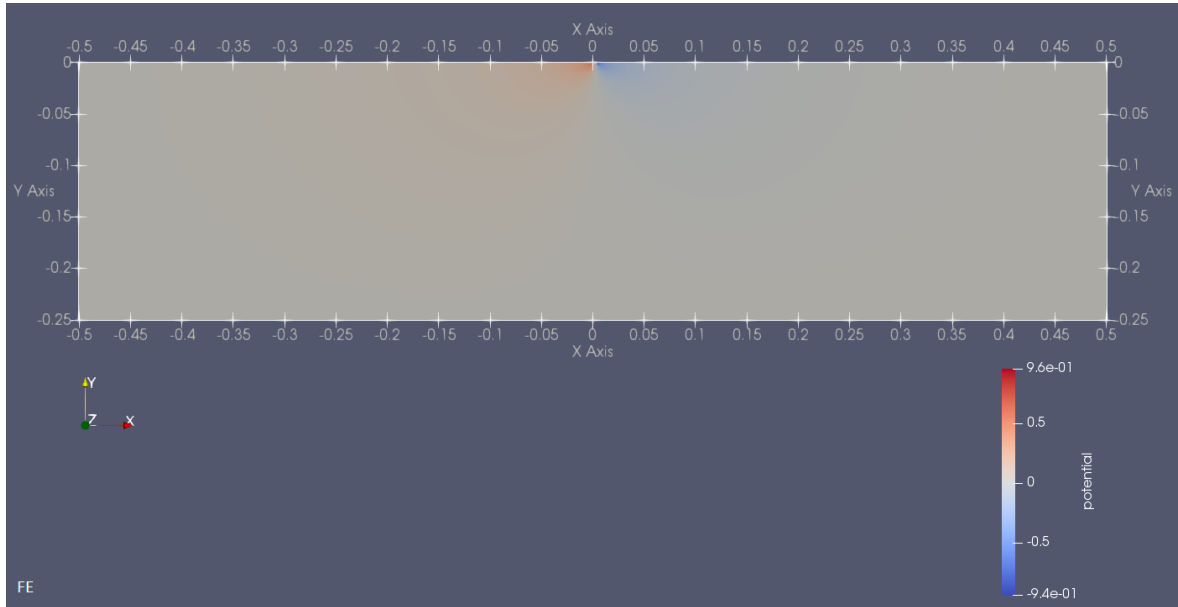**Figure 4-8:** Potential distribution of the FE forward simulation exemplary for the first source position at 0 and $1\ m$. The upper layer has a resistivity of $11.898\ \Omega m$, while the lower layer has a resistivity of $56.933\ \Omega m$.

at the surface. For one full ERT simulation along the whole profile, one forward simulation for each source electrode position needs to be performed. Therefore, 15 forward simulations are computed with the same electrode positions as in the BERT simulation. Exemplary, the potential distribution of the first forward simulation with the source electrode positions at 0 and $1\ m$ is depicted in Figure 4-8. Furthermore, a close-up of the area of interest is shown in Figure 4-9. At first sight, the potential distribution behaves as expected. The potential has in maximum and minimum at the source and sink positions, respectively and decreases in magnitude with further distance from them. But despite that the source and sink inject and eject the same current of $0.1\ A$ and $-0.1\ A$, the resulting magnitude of the positive maximum and negative minimum are not identical. While the maximum has a value of $+0.956699\ V$, the minimum has a value of $-0.943885\ V$. Since they are both located in the same layer with the same resistivity, I do not expect a difference in magnitude.

Furthermore, the potential differences between the potential electrodes of each measurement are calculated and depicted in Figure 4-10. For purposes of comparing, all the three data sets of the BERT, FE and RB simulations are compared in Figure 4-14. When comparing the data sets of BERT and FE, one notices that both data sets follow the same pattern. For each source electrode position, the potential difference decreases with offset. But the magnitude of the data sets vary. While the BERT data set ranges from $4.169 \times 10^{-4}\ V$ to $5.662 \times 10^{-2}\ V$, the FE data set using *DwarfElephant* ranges from $5.478 \times 10^{-3}\ V$ to $8.676 \times 10^{-2}\ V$. Furthermore, the gradient is steeper for the FE data set than in the one simulated in BERT.

Now, I will change my focus on the RB simulations. They require more preparation. As described in Section 2-3-1, the PDE needs to be split up in an parameter-dependent and parameter-independent part. The parameters I am varying are the resistivities ρ of the two layers. I performed the affine decomposition on the weak formulation of the PDE given in Equation 2-16. Note that the volume integrals need to decomposed separately from the

Figure 4-9: A close-up on the area of interest of the potential distribution of FE forward simulation exemplary for the first source position at 0 and $1\ m$. The upper layer has a resistivity of $11.898\ \Omega m$, while the lower layer has a resistivity of $56.933\ \Omega m$.
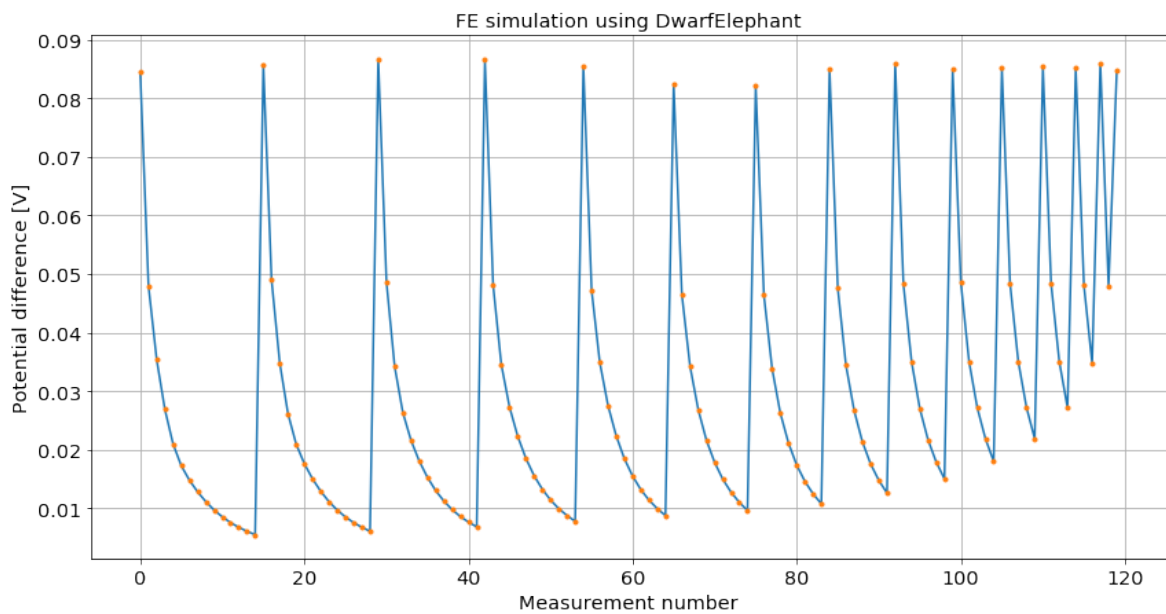
Figure 4-10: Resulting potential differences of the FE forward simulation using *DwarfElephant*. Note that each block represents all measurements with one source position, but varying offsets. Each block starts with a peak.

surface integrals, since the volume integrals are part of the stiffness matrix and the surface integrals are part of the load vector. For both separations, one notices that the only parameter-dependent property is the parameter itself, hence the resistivity ρ.

After the affine decomposition, the offline stage can be performed. Therefore, a training set of parameters need to be defined. I defined the upper bound of the training set by adding 15 % to model resistivities, while I subtracted 15 % from the model resistivities for the lower bounds. Furthermore, an error tolerance between the truth solution and the reduced basis approximation needs to be defined. I set it to a value of 1×10^{-5}. The calculation of the offline stage gives a reduced basis space with 4 basis functions.

Please note that I encountered an error in my simulation in the last days of the project, which remains unsolved until the submission. The error prevents the RB simulations from executing only the online stage with a precomputed reduced basis space. Therefore, for each forward simulation, the reduced basis space needs to computed again in the offline stage. Thus, the described forward simulation of the ERT data set in the following is less efficient than the FE forward simulation.

Since the RB simulation is an approximation to the FE simulation, I used the same simulation specifications. Hence, the same mesh is used, the same boundary conditions are applied with the same values and the source terms are identical. For comparing the results with the FE simulations, the modelled potential distribution with the source and sink located at 0 and 1 m is x-direction is shown in Figure 4-11. Additionally, a close-up on the area of interest is depicted in Figure 4-12. The RB simulation gives similar results as the one computed with the FE method. The electrical field has its maximum and minimum at the source and sink, respectively, and the magnitude of the field decreases with the distance from the source and sink. But by comparing the actual values, one notices differences beyond the defined tolerance. The potential minimum has a value of -0.944155 V, while the maximum is 0.956866 V. For the minima, the error between the FE and the RB simulation is 2.7×10^{-4} V and 1.67×10^{-4} V. Since the error tolerance is defined to be 1×10^{-5}, there needs to be systematic error in the simulations.

Furthermore, the potential difference data set of the RB forward simulation is depicted in Figure 4-13. The RB data set is also compared in the plot in Figure 4-14 with the data sets of the other simulations. The data set of the RB simulation is similar to the one using the FE simulation. But note that the potential differences in the RB data set is for all measurements slightly smaller than the ones of the FE data set.

Nevertheless, an important aspect of the RB method and my project is the computational efficiency. Since I did not achieve a large computation for comparing the computing times of the FE and RB method, I compare the run times of single forward simulations. Using the FE method, one forward simulation takes 1.120091 s. The calculation time of the RB method needs to be distinguished in the run times of the offline and the online stages, because the offline stage usually needs to be calculated only once, while the online stage gives the run time of a single simulation when reduced basis space precomputed in the offline stage. The online stage takes 1.0228×10^{-2} s, while the offline stage requires 9.77001 s The gives a speed-up of 109.512, which is calculated by dividing the time of the FE simulation by the time of the online stage. Furthermore, the pay-off, which gives the number of simulations, when the use of the RB method is faster than the simulations of the FE method. The pay-off has a value of 8.803. This calculations assume that the offline stage only needs to be calculated once.

Figure 4-11: Potential distribution of the RB forward simulation exemplary for the first source position at 0 and $1\ m$. The upper layer has a resistivity of $11.898\ \Omega m$, while the lower layer has a resistivity of $56.933\ \Omega m$.
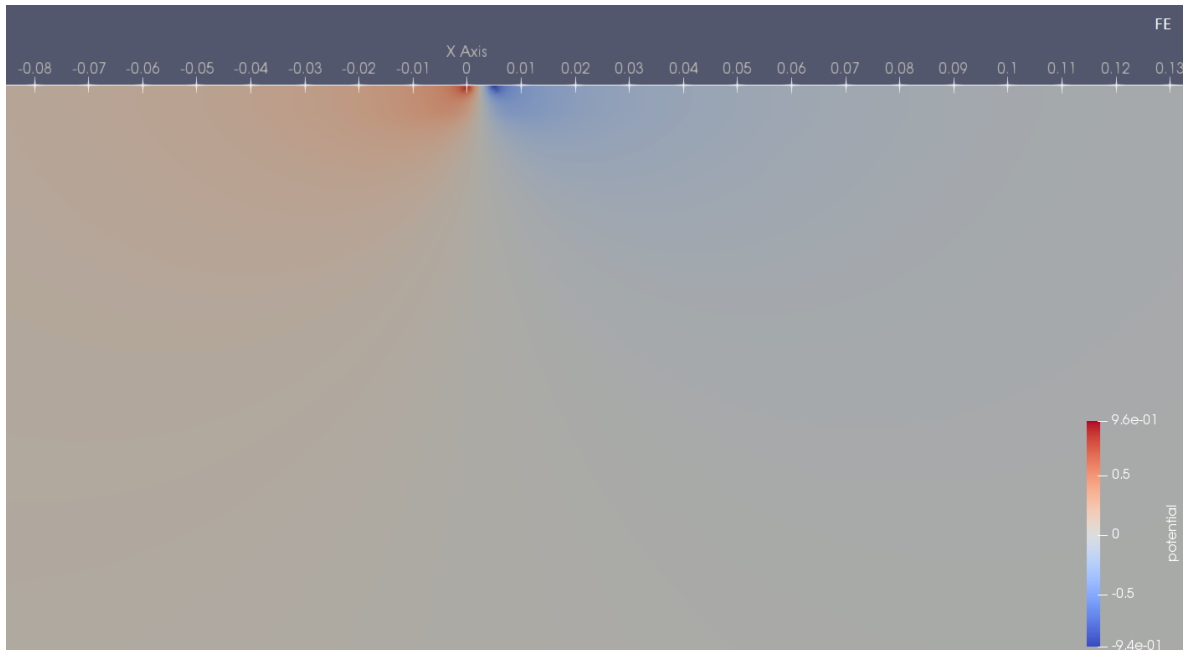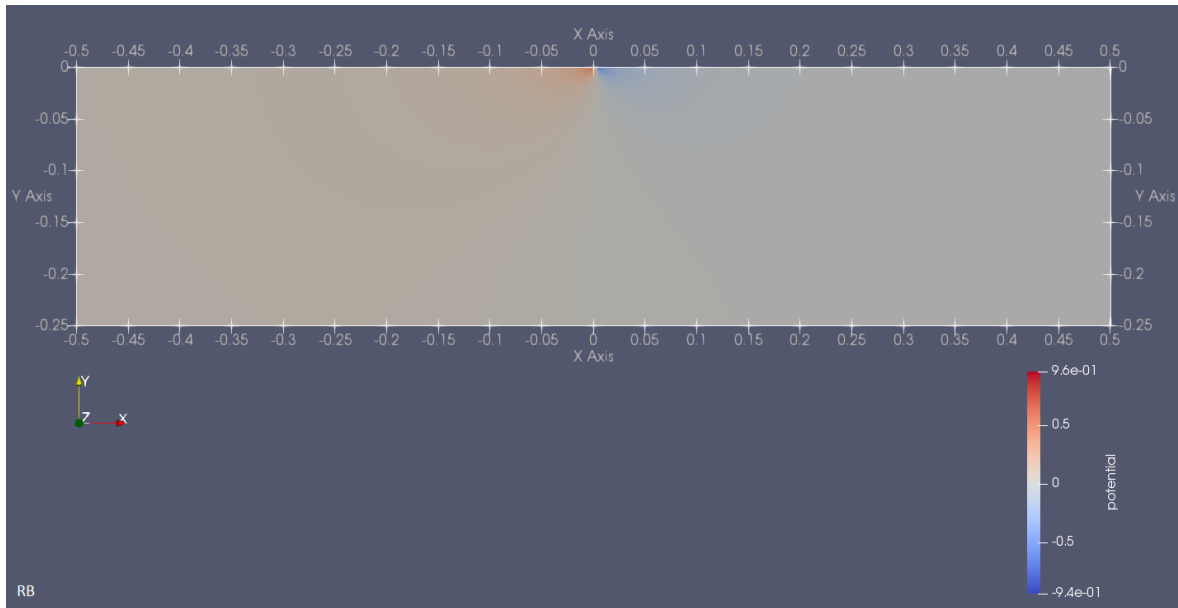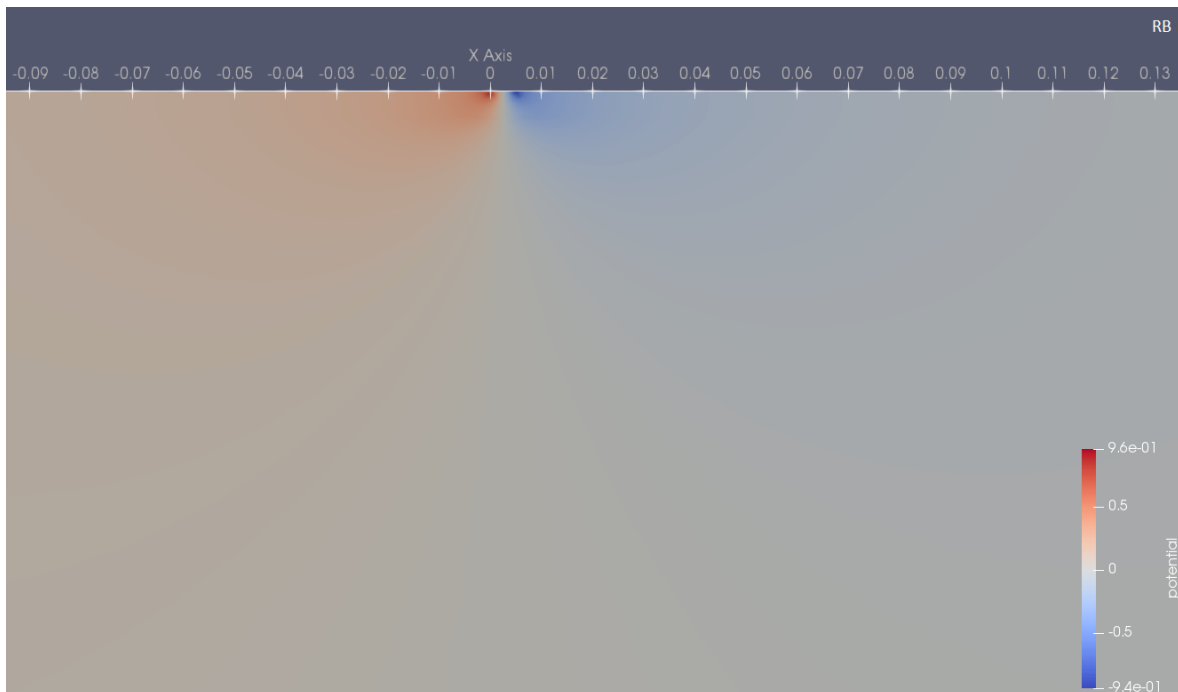

Figure 4-12: A close-up on the area of interest of the potential distribution of RB forward simulation exemplary for the first source position at 0 and $1\ m$. The upper layer has a resistivity of $11.898\ \Omega m$, while the lower layer has a resistivity of $56.933\ \Omega m$.
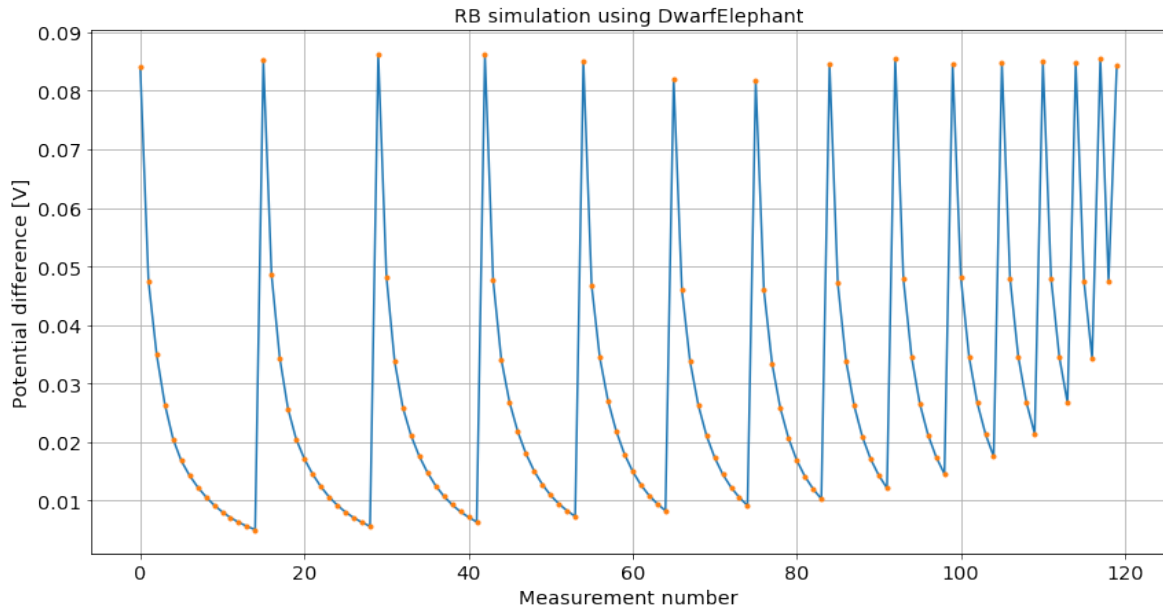
Figure 4-13: Resulting potential differences of the RB forward simulation using *DwarfElephant*. Note that each block represents all measurements with one source position, but varying offsets. Each block starts with a peak.
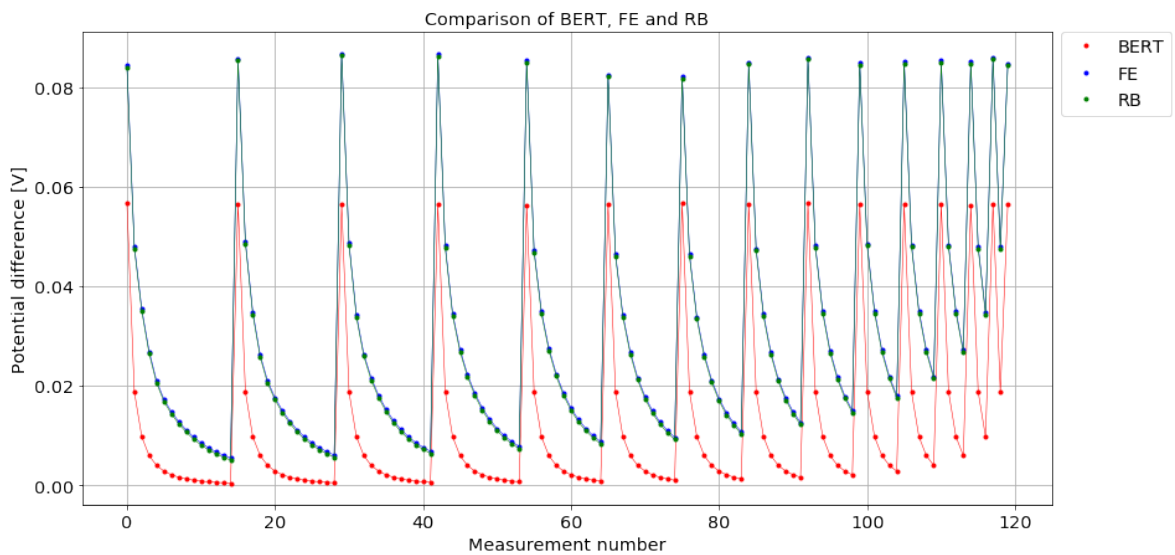
Figure 4-14: Comparison of the potential differences of the forward simulations using FE (yellow) and RB (green) with the aid of *DwarfElephant* and the forward simulation of BERT(blue).

4-3   Uncertainty quantification results

Unfortunately, no uncertainty quantification has been calculated. One of the original purposes of the uncertainty quantifications in this project was to investigate the uncertainties induced by the inversion process. Due to the error, which prevents the RB simulation from executing the offline stage only, the uncertainty quantification using RB would be meaningless. But an uncertainty quantification using FE method could have been performed, but there was no time left. With more time, I could have at least find answers regarding the question of induced uncertainties.

Chapter 5

Discussion

The major objective of the project is to investigate if and how the RB method can be used for ERT simulations to increase their computational efficiency. Therefore, I compared the simulations using the RB method with simulations using the FE method. These simulations are supposed to be used in an inversion and an uncertainty quantification for examining the required computational effort. Furthermore, the uncertainty quantification has the purpose of surveying the induced uncertainties by the inversion process in BERT. Unfortunately, the time of the project ran out and I was unable to perform neither the inversion nor the uncertainty quantification. Furthermore, during the last days of the project, an error became apparent in the RB problem. This error prevents the online stage from being executed only. This makes my RB simulation less efficient than the FE simulation. In the following, I will discuss the results and the problems occurred during the project.

The generation of the synthetic data set in BERT and the following inversion performed both quite well, but since the initial model is rather simple, I did not expect major problems in the process. The data sets obtained from the BERT and the FE forward simulation show the same trend. With increasing offset between the source and the potential electrodes, the potential differences decrease. From a physical perspective, I expect such a behaviour. Since the potentials themselves decrease with the distance, the differences become smaller to. But the gradient of this trend differs for the two data sets. For smaller offset, the potential differences in the BERT have a stronger gradient than in the FE data set, but for larger offsets the gradient of the FE data set becomes stronger than the gradient of the BERT data set. These differences may occur, because the mathematics behind the simulations vary. For example, the BERT simulation uses an approach including the calculation of the total potential and a secondary potential, while my FE simulation only calculates the total potential. Furthermore, different models are used, which contribute to the different outcome. While the BERT simulation uses the initial model, which I presented in Section 3-2, the FE simulation uses the model, which is generated on the base of the inversion result. The initial model has resistivities of 10 Ωm and 100 Ωm for the upper and lower layers, respectively, while the resistivities obtained from the inversion process are 11.898 Ωm and 56.933 Ωm for the upper and the lower layer, respectively. While the resistivity of the upper layer in the new model is quite similar to the one of the initial model, the resistivity of the lower

layer is remarkably smaller. Furthermore, there occur differences in the magnitudes of the potential differences. They may occur due to different source and sink currents. The currents are not clearly defined in the published papers introducing the software package BERT [Rücker et al., 2006][Günther et al., 2006]. Since there is no current, which is optimal for any model, I would expect the currents chosen in BERT to have a value of 1 with a decimal power. For example, values like ± 0.01 A, ± 0.1 A or ± 1 A and no arbitrary value. For investigating this, I tested different currents. The best tested value appears to be ± 0.066 A. Since there are other dissimilarities in the simulations like the model and the mathematical approaches, I do not expect to recover exactly the same values. Trying to fit the data neglecting the impact of other factors, I decided that a value of ± 0.1 A appears to be more reasonable. Note that the current of ± 0.066 A does not fit the dissimilarities in the gradients. Another possible origin of the deviations between the BERT and FE data sets is an incorrectly implementation of the non-dimensionalized model lengths into the PDE. If a source and sink current of ± 1 V is selected and the resulting FE data are scaled down by the non-dimensionalization factor of 200, the data are in a similar range as the ones obtained from BERT. This may be coincidental, but can also be the reason for the mismatch. Further error evaluation needs to be done here. An additional uncertainty quantification investigating the source and sink currents may give more insights.

Beside the dissimilarities between the data sets of BERT and FE, also the FE and RB simulations do not show the desired similarity. Despite an error tolerance of 1×10^{-5} is defined in the generation of the reduced basis space, the error between the FE and RB reaches values above 1×10^{-4}. I would expect the error to occur, because I have a systematic error in my problem formulation in the simulation software *DwarfElephant*. Inserting the decomposed PDE correctly into the simulation is no straightforward task and I expect that I did not accomplish it appropriately.

At the end of the project, I discovered a conceptual inefficiency in my project. I only considered the resistivity as a varying parameter in the RB method. But ERT measurements require multiple source positions. Hence, it would be very helpful to implement the source position as a varying parameter too. With only the resistivity as a varying parameter, one reduced basis space would need to be generated for each source position. For my measurement configuration, the offline stage need to be calculated 15 times. This reduces the efficiency of the RB method. Therefore, for a proper use of the RB method, the source position needs to be a varying parameter too. So, in my approach the reduced basis space needs to be calculated 15 times, once for each source position. But that is only a workaround, I expect to be significantly less efficient than the one considering the source position as a varying parameter.

The uncertainty quantification has not been performed, due to the lack of time. It was supposed to investigate the resistivity values. Since the resistivities of the lower layer differ significantly in the two models, I also expect the obtained value from the inversion to be quite uncertain. However, the resistivity values of the upper layer are quite similar, so I expect the uncertainty quantification to evaluate it to be quite certain. Since the model of the two simulations differ, I expect also some minor uncertainties originating from these differences.

The speed-up of using the RB method instead of the FE method is with a value of 109.512 a remarkable improvement. Since the reduced basis space contains 4 basis functions, I expected a significant value. Also the pay-off of 8.803 is quite low. This pay-off would even reduce the computing time of a full ERT data set using the rather small measurement configuration used in this project. For larger computations the use of the RB method can reduce the computing time significantly.

Chapter 6

Conclusion

Summarizing, I see a place of the reduced basis method (RB) in the practical application of the electrical resistivity tomography. The full simulation of RB measurements requires the calculation of multiple forward simulations, one for each source position. For my approach without varying the source positions, the offline stage needs to be calculated once for each source position, which limits the efficiency increase by the use of RB. Now, I would suggest to include the source position as a varying parameter in the RB method. Then, the offline stage would only need to be computed once and the computational efficiency would increase even more. This is especially advantageous, if the Wenner configuration is used, instead of the Dipole-Dipole configuration in this project. The Wenner configuration allows only a single measurement per source electrode position, while the Schlumberger and the Dipole-Dipole configuration allow multiple measurements. For large calculations like uncertainty quantifications or the inversion of field data, the expected reduction in computing time would be significant. But note that the use of the RB method requires more effort in the implementation. Hence, it always needs to be evaluated if the planned computation is large enough that the use of RB pays off. Unfortunately, I did not achieved my aims for the project to prove the full potential of the RB method for the ERT problem, by performing either an inversion or an uncertainty quantification using RB simulations. But hopefully my results will help in upcoming research to be more successful.

The next step of upcoming research would be to vary not just the resistivities, but also the source position in the RB. This would increase the potential of the technique even more. Additionally, the implementation of the RB method into the inversion process is an important step, since the inversion is a necessary processing step for data of most ERT field measurements. Furthermore, the RB method could be implemented in optimizing the field measurements by enabling an inversion of measured data directly in the field. Then the measurement configuration and parameters could be modified to improve the outcoming results.

Bibliography

[Adams et al., 2014] Adams, B., Ebeida, M., Eldred, M., Geraci, G., Jakeman, J., Maupin, K., Monschke, J., Stephens, J., Swiler, L., Vigil, D., Wildey, T., Bohnhoff, W., Dalbey, K., Eddy, J., Frye, J., Hooper, R., Hu, K., Hough, P., Khalil, M., Ridgway, E., Winokur, J., and Rushdi, A. (2014). *Dakota, A Multilevel Parallel Object-Oriented Framework for Design Optimization, Parameter Estimation, Uncertainty Quantification, and Sensitivity Analysis: Version 6.8 Users Manual.* Sandia National Laboratories, Albuquerque, NM, USA. Updated May 8, 2018. Available online from http://dakota.sandia.gov/documentation.html.

[Bardsley, 2012] Bardsley, J. M. (2012). Mcmc-based image reconstruction with uncertainty quantification. *SIAM Journal on Scientific Computing*, 34(3):A1316–A1332.

[Bellman and Casti, 1971] Bellman, R. and Casti, J. (1971). Differential quadrature and long-term integration. *Journal of Mathematical Analysis and Applications*, 34(2):235–238.

[Binev et al., 2011] Binev, P., Cohen, A., Dahmen, W., DeVore, R., Petrova, G., and Wojtaszczyk, P. (2011). Convergence rates for greedy algorithms in reduced basis methods. *SIAM journal on mathematical analysis*, 43(3):1457–1472.

[Boyaval et al., 2009] Boyaval, S., Le Bris, C., Maday, Y., Nguyen, N. C., and Patera, A. T. (2009). A reduced basis approach for variational problems with stochastic parameters: Application to heat conduction with variable robin coefficient. *Computer Methods in Applied Mechanics and Engineering*, 198(41-44):3187–3206.

[Buffa et al., 2012] Buffa, A., Maday, Y., Patera, A. T., Prudhomme, C., and Turinici, G. (2012). A priori convergence of the greedy algorithm for the parametrized reduced basis method. *ESAIM: Mathematical modelling and numerical analysis*, 46(3):595–603.

[Burger, 1992] Burger, H. R. (1992). *Exploration geophysics of the shallow subsurface.* Englewood Cliffs, NJ (United States); Prentice Hall.

[Casenave et al., 2015] Casenave, F., Ern, A., and Lelièvre, T. (2015). A nonintrusive reduced basis method applied to aeroacoustic simulations. *Advances in Computational Mathematics*, 41(5):961–986.

[Chen et al., 2009] Chen, Y., Hesthaven, J. S., Maday, Y., and Rodríguez, J. (2009). Improved successive constraint method based a posteriori error estimate for reduced basis approximation of 2d maxwell's problem. *ESAIM: Mathematical Modelling and Numerical Analysis*, 43(6):1099–1116.

[Chen et al., 2010] Chen, Y., Hesthaven, J. S., Maday, Y., and Rodríguez, J. (2010). Certified reduced basis methods and output bounds for the harmonic maxwell's equations. *SIAM Journal on Scientific Computing*, 32(2):970–996.

[de Orio, 2001] de Orio, R. (2001). *Electromigration Modeling and Simulation*. phdthesis, TU Wien.

[Donea and Huerta, 2003] Donea, J. and Huerta, A. (2003). *Finite element methods for flow problems*. John Wiley & Sons.

[Fares et al., 2011] Fares, M., Hesthaven, J. S., Maday, Y., and Stamm, B. (2011). The reduced basis method for the electric field integral equation. *Journal of Computational Physics*, 230(14):5532–5555.

[Ford, 2005] Ford, E. B. (2005). Quantifying the uncertainty in the orbits of extrasolar planets. *The Astronomical Journal*, 129(3):1706.

[Gaston et al., 2009] Gaston, D., Newman, C., Hansen, G., and Lebrun-Grandie, D. (2009). Moose: A parallel computational framework for coupled systems of nonlinear equations. *Nuclear Engineering and Design*, 239(10):1768–1778.

[Geuzaine and Remacle, 2009] Geuzaine, C. and Remacle, J.-F. (2009). Gmsh: A 3-d finite element mesh generator with built-in pre-and post-processing facilities. *International journal for numerical methods in engineering*, 79(11):1309–1331.

[Günther and Rücker, 2017] Günther, T. and Rücker, C. (2017). *Boundless Electrical Resistivity Tomography BERT 2 -the user tutorial*. Version 2.2.3. Available on "www.resisitivity.net/download/bert_tutorial.pdf".

[Günther et al., 2006] Günther, T., Rücker, C., and Spitzer, K. (2006). Three-dimensional modelling and inversion of dc resistivity data incorporating topographyii. inversion. *Geophysical Journal International*, 166(2):506–517.

[Hesthaven et al., 2016] Hesthaven, J. S., Rozza, G., Stamm, B., et al. (2016). *Certified reduced basis methods for parametrized partial differential equations*. Springer.

[Hesthaven et al., 2012] Hesthaven, J. S., Stamm, B., and Zhang, S. (2012). Certified reduced basis method for the electric field integral equation. *SIAM Journal on Scientific Computing*, 34(3):A1777–A1799.

[Kemna, 2000] Kemna, A. (2000). *Tomographic inversion of complex resistivity: Theory and application*. Der Andere Verlag Osnabruck, Germany.

[Lassila et al., 2013] Lassila, T., Manzoni, A., Quarteroni, A., and Rozza, G. (2013). A reduced computational and geometrical framework for inverse problems in hemodynamics. *International journal for numerical methods in biomedical engineering*, 29(7):741–776.

[Lowrie, 2007] Lowrie, W. (2007). *Fundamentals of geophysics*. Cambridge university press, 2nd edition.

[Manzoni et al., 2014] Manzoni, A., Lassila, T., Quarteroni, A., and Rozza, G. (2014). A reduced-order strategy for solving inverse bayesian shape identification problems in physiological flows. In *Modeling, Simulation and Optimization of Complex Processes-HPSC 2012*, pages 145–155. Springer.

[McGillivray and Oldenburg, 1990] McGillivray, P. R. and Oldenburg, D. W. (1990). Methods for calculating fréchet derivatives and sensitivities for the non-linear inverse problem: A comparative study. *Geophysical Prospecting*, 38(5):499–524.

[Prud'Homme et al., 2002] Prud'Homme, C., Rovas, D. V., Veroy, K., Machiels, L., Maday, Y., Patera, A. T., and Turinici, G. (2002). Reliable real-time solution of parametrized partial differential equations: Reduced-basis output bound methods. *Journal of Fluids Engineering*, 124(1):70–80.

[Rozza, 2005a] Rozza, G. (2005a). On optimization, control and shape design of an arterial bypass. *International Journal for Numerical Methods in Fluids*, 47(10-11):1411–1419.

[Rozza, 2005b] Rozza, G. (2005b). Shape design by optimal flow control and reduced basis techniques. Technical report, EPFL.

[Rücker et al., 2006] Rücker, C., Günther, T., and Spitzer, K. (2006). Three-dimensional modelling and inversion of dc resistivity data incorporating topographyi. modelling. *Geophysical Journal International*, 166(2):495–505.

[Rücker et al., 2017] Rücker, C., Günther, T., and Wagner, F. M. (2017). pygimli: An open-source library for modelling and inversion in geophysics. *Computers & Geosciences*, 109:106–123.

[Schiavazzi et al., 2016] Schiavazzi, D., Arbia, G., Baker, C., Hlavacek, A. M., Hsia, T.-Y., Marsden, A., Vignon-Clementel, I., and of Congenital Hearts Alliance (MOCHA) Investigators, T. M. (2016). Uncertainty quantification in virtual surgery hemodynamics predictions for single ventricle palliation. *International journal for numerical methods in biomedical engineering*, 32(3):e02737.

[Schwarz and Köckler, 2011] Schwarz, H. R. and Köckler, N. (2011). *Numerische Mathematik*. Vieweg+Teubner Verlag, 8 edition.

[Si, 2003] Si, H. (2003). Tetgen: A 3d delaunay tetrahedral mesh generator.

[Telford et al., 1990] Telford, W. M., Geldart, L. P., and Sheriff, R. E. (1990). *Applied geophysics*, volume 1. Cambridge university press.

[Veroy et al., 2003] Veroy, K., Prud'Homme, C., Rovas, D., and Patera, A. (2003). A posteriori error bounds for reduced-basis approximation of parametrized noncoercive and nonlinear elliptic partial differential equations. page 3847.

[Vrugt et al., 2009] Vrugt, J. A., Ter Braak, C., Diks, C., Robinson, B. A., Hyman, J. M., and Higdon, D. (2009). Accelerating markov chain monte carlo simulation by differential evolution with self-adaptive randomized subspace sampling. *International Journal of Nonlinear Sciences and Numerical Simulation*, 10(3):273–290.

[Wei and Versteeg, 2008] Wei, S. and Versteeg, R. (2008). *A Fast Forward Modeling Algorithm for ERT Inversion*, pages 596–606.